Available online at www.sciencedirect.com

ScienceDirect

Coordination Chemistry Reviews 251 (2007) 557–576

COORDINATION CHEMISTRY REVIEWS

www.elsevier.com/locate/ccr

Review

Electronic transitions and bonding properties in a series of five-coordinate "16-electron" complexes $[Mn(CO)_3(L_2)]^-$ (L_2 = chelating redox-active π-donor ligand)

František Hartl [a,*], Patrick Rosa [b], Louis Ricard [b], Pascal Le Floch [b], Stanislav Záliš [c,**]

[a] *Van't Hoff Institute for Molecular Sciences, Universiteit van Amsterdam, Nieuwe Achtergracht 166, 1018 WV Amsterdam, The Netherlands*
[b] *Laboratoire "Hétéroéléments et Coordination", UMR CNRS 7653, DCPH, Ecole Polytechnique, 91128 Palaiseau Cedex, France*
[c] *J. Heyrovský Institute of Physical Chemistry, Academy of Sciences of the Czech Republic, Dolejškova 3, 182 23 Prague 8, Czech Republic*

Received 5 June 2006; accepted 5 September 2006
Available online 9 September 2006

Dedicated to Professor James J. Turner on his 70th birthday.

Contents

Abstract

In this article we present for the first time accurate density functional theory (DFT) and time-dependent (TD) DFT data for a series of electronically unsaturated five-coordinate complexes $[Mn(CO)_3(L_2)]^-$, where L_2 stands for a chelating strong π-donor ligand represented by catecholate, dithiolate, amidothiolate, reduced α-diimine (1,4-dialkyl-1,4-diazabutadiene (R-DAB), 2,2′-bipyridine) and reduced 2,2′-biphosphinine types. The single-crystal X-ray structure of the unusual compound $[Na(BPY)][Mn(CO)_3(BPY)]\cdot Et_2O$ and the electronic absorption spectrum of the anion $[Mn(CO)_3(BPY)]^-$ are new in the literature. The nature of the bidentate ligand determines the bonding in the complexes, which varies between two limiting forms: from completely π-delocalized diamagnetic $\{(CO)_3Mn–L_2\}^-$ for L_2 = α-diimine or biphosphinine, to largely valence-trapped $\{(CO)_3Mn^I–L_2{}^{2-}\}^-$ for $L_2{}^{2-}$ = catecholate, where the formal oxidation states of Mn and L_2 can be assigned. The variable degree of the π-delocalization in the $Mn(L_2)$ chelate ring is indicated by experimental resonance Raman spectra of $[Mn(CO)_3(L_2)]^-$ (L_2 = 3,5-di-*t*Bu-catecholate and *i*Pr-DAB), where accurate assignments of the diagnostically important Raman bands have been aided by vibrational analysis. The L_2 = catecholate type of complexes is known to react with Lewis bases (CO substitution, formation of six-coordinate adducts) while the strongly π-delocalized complexes are inert. The five-coordinate complexes adopt usually a distorted square pyramidal geometry in the solid state, even though transitions to a trigonal bipyramid are also not rare. The experimental structural data and the corresponding DFT-computed values of bond

---

[*] Corresponding author. Tel.: +31 20 525 6450; fax: +31 20 525 6456.
[**] Corresponding author. Tel.: +420 266 053 268; fax: +420 286 586 307.
E-mail addresses: hartl@science.uva.nl (F. Hartl), stanislav.zalis@jh-inst.cas.cz (S. Záliš).

doi:10.1016/j.ccr.2006.09.003

lengths and angles are in a very good agreement. TD-DFT calculations of electronic absorption spectra of the studied Mn complexes and the strongly π-delocalized reference compound [Fe(CO)$_3$(Me-DAB)] have reproduced qualitatively well the experimental spectra. Analyses of the computed electronic transitions in the visible spectroscopic region show that the lowest-energy absorption band always contains a dominant (in some cases almost exclusive) contribution from a π(HOMO) → π*(LUMO) transition within the MnL$_2$ metallacycle. The character of this optical excitation depends strongly on the composition of the frontier orbitals, varying from a partial L$_2$ → Mn charge transfer (LMCT) through a fully delocalized π(MnL$_2$) → π*(MnL$_2$) situation to a mixed (CO)Mn → L$_2$ charge transfer (LLCT/MLCT). The latter character is most apparent in the case of the reference complex [Fe(CO)$_3$(Me-DAB)]. The higher-lying, usually strongly mixed electronic transitions in the visible absorption region originate in the three lower-lying occupied orbitals, HOMO − 1 to HOMO − 3, with significant metal-d contributions. Assignment of these optical excitations to electronic transitions of a specific type is difficult. A partial LLCT/MLCT character is encountered most frequently. The electronic absorption spectra become more complex when the chelating ligand L$_2$, such as 2,2′-bipyridine, features two or more closely spaced low-lying empty π* orbitals.

Keywords: Manganese carbonyl; π-Donor ligand; Electronic delocalization; Five-coordinate complex; Crystal structure; Density functional theory; Electronic absorption spectrum; Resonance Raman

---

1. Introduction

Much attention has been devoted to coordinatively and electronically unsaturated transition metal complexes due to the involvement of many of them in catalytic cycles. Among typical examples belong coordinatively unsaturated two- or three-legged piano stool (i.e., cyclopentadienyl or arene) complexes with 16 valence electrons, which are stabilized by coordination of π-donor ligands [1,2]. The incorporation of π-donor alkoxide co-ligands was used to prepare unsaturated polyhydride complexes such as [Ir^{III}H$_2$(OR)(P*i*Pr$_3$)$_2$] which is much more reactive than [Ir^{III}H$_3$(P*i*Pr$_3$)$_3$] with 18 valence electrons [3,4].

Density functional theory (DFT) studies of a series of *group-6* 18e complexes [M(CO)$_5$X]$^-$ (M = Cr, Mo, W; X = a good π-donor ligand like NH$_2$$^-$, NHR$^-$, OH$^-$, OR$^-$ or halide) have shown that the π-donation from X induces some σ-antibonding interaction between M and the cis CO ligands. It also causes d/p orbital mixing (hybridization) at the metal center, which reduces cis M–CO π-back-donation. Both effects are responsible for strongly labilized cis M–CO bonds and dissociation of a cis CO ligand. The resulting 16e species are stabilized by the π-donation from the lone-pair p$_\pi$ orbital of the ligand X to the π-acceptor orbital of the {M(CO)$_4$} fragment [5,6]. A similar situation applies for complexes [Mn(CO)$_5$X] (X = e.g., Cl$^-$) [7].

An interesting example of an electron-deficient group-6 metal complex is [W(CO)$_3$(C$_2$H$_2$)], where the acetylene ligand acts as a four-electron donor after CO dissociation from parent [W(CO)$_4$(C$_2$H$_2$)], employing also its out-of-plane $\pi_\perp$-donor orbital [6,8].

In the past 2 decades, considerable attention was paid to group-6 carbonyl complexes with chelating π-donor ligands. To the best of our knowledge, the first complex of this type, [Cr(CO)$_3$(1,2-S,S-C$_6$H$_4$)]$^{2-}$ (1,2-S,S-C$_6$H$_4$ stands for benzene-1,2-dithiolate), was published in 1985 by Sellmann et al., including the crystal structure. This five-coordinate Cr species with formal 16e configuration was found highly reactive towards CO or NO$^+$, producing 18e complexes [9]. In the following paper, Sellmann et al., described a full series of formally Cr(0), Mo(0) and W(0) tricarbonyl dithiolate complexes with various substituents on the dithiolate ring, and also complexes with aliphatic 1,2-dithiolates. The presence of electron-withdrawing chloro substituents or methylation of the donor sulfur atoms reduces significantly the π-donor ability of the dithiolate ligand, so that 18e tetracarbonyl species could also be isolated. The six-coordinate 18e tetracarbonyl Mo and W complexes are considerably more stable than the Cr compounds and do not split off CO readily [10]. The increasing size of the heavier transition metal atom is an important factor contributing to the 3d–5d periodic trends of this kind, with more examples given below.

Starting in 1992, Darensbourg et al., reported a series of similar group-6 zerovalent metal tricarbonyl complexes with catecholate ligands (1,2-O,O-C$_6$H$_4$ = CAT) [11–13]. The reactivity trends, determined by the extent of the π-donation and the metal size, resemble those in the dithiolate series. For example, [Cr(CO)$_3$(CAT)]$^{2-}$ is unreactive towards P(OMe)$_3$ at room temperature while the larger Mo and W metal centers react with P(OMe)$_3$ even when donor *t*Bu substituents are bound at the catecholate ring (3,5-di-*t*Bu-1,2-O,O-C$_6$H$_4$ = *t*Bu-CAT). The same difference exists in the case of CO coordination: while [Cr(CO)$_3$(*t*Bu-CAT)]$^{2-}$ is completely inert at modest CO pressures, W forms a stable tetracarbonyl complex under a CO atmosphere and Mo is an intermediate case, the tricarbonyl and tetracarbonyl species being in equilibrium. After the catecholate series, Darensbourg et al., continued the structural and spectroscopic investigation of group-6 complexes [M(CO)$_3$(1,2-E,E′-C$_6$H$_4$)]$^{2-}$ with other E,E′ combinations of the π-donor groups: O,S; O,NH; NH,NH; S,NH. Attempts to prepare a tungsten complex with the deprotonated 1,2-diphosphinobenzene ligand (E,E′ = PH,PH) were not successful. Experimental results and ab initio theoretical calculations have demonstrated that the π-donation and stabilization of the coordinatively unsaturated 16e complexes increases in the order NH,NH < O,NH < O,O < S,NH < O,S < S,S [14,15].

No attempts have been made so far to prepare and investigate this type of group-6 complexes with widely used α-diimine ligands; although, [Cr(CO)$_3$(BPY)]$^{2-}$ (BPY = 2,2′-bipyridine) was observed with IR spectroelectrochemistry as a two-electron reduction product of [Cr(CO)$_4$(BPY)] [16].

The work on group-6 complexes with formally d^6 transition metal centers inspired Liaw and co-workers to extend the spectroscopic and crystallographic studies to *group-7*, namely

d^6 Mn complexes. Among a great variety of compounds prepared, a dominant position was devoted to five-coordinate anions $[Mn(CO)_3(1,2\text{-}E,E'\text{-}C_6H_4)]^-$, where E,E′ are the following bidentate combinations: S,S; S,NH; Se,NH; Te,NH; S,O and O,O. According to IR ν(CO) spectroscopic data, the ligand π-donor ability was found to increase in the order O,O < S,O < S,S < S,NH < Se,NH < Te,NH. Curiously, the catecholate complex $[Mn(CO)_3(CAT)]^-$ (CAT = 1,2-O,O-C_6H_4) is unstable at room temperature and could not be isolated [17–19]. Recently, Sweigart et al., prepared and characterized a stable isomer of the latter complex. Its crystal structure has revealed that this remarkable compound can be formulated as 1,2-benzoquinone η^4-π-bound to the $\{Mn(CO)_3\}^-$ moiety. The quinone oxygen atoms interact with the $[Na(H_2O)_3]^+$ counterion [20]. However, the first stable five-coordinate Mn catecholate complexes of this class, $[Mn(CO)_2(L)(t\text{Bu-CAT})]^-$ (L = CO, $P(OEt)_3$) were prepared and thoroughly characterized, including the crystal structure of the tricarbonyl anion and electronic absorption spectra, already in early 1990s by Hartl et al. The stabilizing (partial) π-delocalization within the Mn-catecholate chelate ring has been proven by resonance Raman spectroscopy [21–25]. The corresponding 5d Re catecholate complexes were found to exist exclusively as stable six-coordinate 18e compounds. This observation agrees with the 3d–5d periodic trends reported [26] for the catecholate complexes of the group-6 metals (see above). The valence-localized concept is valid in this case, as indicated [22,23] by the formation of the one-electron-reduced d^7 Mn-localized radical $[Mn^0(CO)_3(t\text{Bu-CAT})]^{2-}$. The corresponding one-electron-oxidized five-coordinate complex with the radical semiquinone ligand (*t*Bu-SQ) lacking the π-donor properties is unfortunately too reactive and could not be characterized [22,24] by spectroscopic techniques. Hartl et al. also investigated an important group of strongly π-delocalized anions $[Mn(CO)_3(L_2)]^-$ with chelating L_2 = 2,2′-bipyridine (BPY), 1,4-di-isopropyl-1,4-diazabutadiene (*i*Pr-DAB) and 4,4′,5,5′-tetramethyl-2,2′-biphosphinine (TMBP). These compounds were prepared by two-electron reduction of precursor halide complexes [27–29]. The crystal structure of air and moisture-sensitive $[Mn(CO)_3(BPY)]^-$ is presented in a following section, that of $[Mn(CO)_3(TMBP)]^-$ has been published elsewhere [29]. The corresponding anionic rhenium α-diimine complexes are also well known. The electronic π-delocalization stabilizing the five-coordinate geometry of $[Re(CO)_3(\alpha\text{-diimine})]^-$ increases with the basicity of the α-diimine ligand [30,31]. One of the more investigated complexes in this series is $[Re(CO)_3(BPY)]^-$. This complex is well known as an efficient catalyst of electrochemical reduction of carbon dioxide [32]. In acetonitrile, it exists at room temperature in a mixture with six-coordinate $[Re(MeCN)(CO)_3(BPY)]^-$. The equilibrium shifts completely towards the latter anion at sufficiently low temperatures. Also $[Re\{P(OEt)_3\}(CO)_3(BPY)]^-$ was formed electrochemically at room temperature [32,33]. This behavior has not been observed for $[Mn(CO)_3(BPY)]^-$ that only exists in the five-coordinate geometry and is completely unreactive towards carbon dioxide. Recently, the electronic absorption spectrum of $[Re(CO)_3(BPY)]^-$ was analyzed by time-dependent density functional theory (TD-DFT) calculations [34].

Examples of electron-deficient five-coordinate complexes of *group-8* metals are rare. Among them we place $[Fe(CO)_2(CN)(1,2\text{-}S,NH\text{-}C_6H_4)]^-$, which is a starting compound for functional models of the dinuclear iron active sites of [Fe]-only hydrogenases) [35], and the photochemically prepared related complex $[Fe(CO)(CN)_2(S,N\text{-}C_5H_4)]^-$ (S,N-C_5H_4 = 2-pyridinethiolate anion) [36]. Series of 2e-reduced ruthenium compounds of the type $[Ru(CO)_2(L)(\alpha\text{-diimine})]^-$ (L = alkyl, $EPh_3{}^-$ (E = Ge, Sn, Pb) and $\{Ru(CO)_2(\eta^5\text{-}C_5H_5)\}^-$; α-diimine = *i*Pr-DAB, BPY) also belong to this class of formally d^6 metal complexes [37–39].

It is of interest to unravel whether representatives of another series of group-8 complexes, $[M(CO)_3(\alpha\text{-diimine})]$ (M = Fe, Ru; α-diimine = e.g., R-DAB, BPY) [40] can be described as valence-trapped 18e $\{M^0\text{–}(\alpha\text{-diimine})\}$ or electron-deficient $\{M^{\delta+}\text{–}(\alpha\text{-diimine}^{\delta-})\}$ compounds stabilized by π-delocalization within the M(α-diimine) chelate ring. The extreme charge-separated 16e $\{M^{II}\text{–}(\alpha\text{-diimine}^{2-})\}$ alternative is highly unlikely.

One example of strongly π-delocalized five-coordinate complex of *group-9* metals is $[Co(triphos)(t\text{Bu-CAT})]^+$; triphos standing for $MeC(CH_2PPh_2)_3$ capable of stabilizing five-coordinate geometries [41]. This compound is completely inert towards an uptake and transfer of dioxygen. The π-delocalization within the metal-catecholate chelate ring decreases when proceeding to the corresponding rhodium and iridium complexes. Strong evidence for this trend has been obtained from the resonance Raman spectra, comparison of redox properties and increasing affinity towards dioxygen and Lewis bases [42]. The metal dependence fully complies with the general behavior of the five-coordinate, formally 16e complexes of chelated 3d–5d metals from the different groups of the periodic table, as illustrated above. The increasing size of 4d and 5d metal centers and larger ligand-field splitting between the d-levels, causing worse energy matching with frontier orbitals of the non-innocent ligand, are the main factors accounting for the observed differences in the extent of the π-delocalization and, consequently, in the stability of the five-coordinate geometry versus uptake of a sixth ligand. More details are given in Fig. 1.

In the literature, quite a large number of crystal structures, spectroscopic (NMR, IR, Raman) and electrochemical properties and reactivity of the electron-deficient five-coordinate complexes stabilized by chelating π-donor ligands have been reported so far. On the other hand, there has been an apparent lack of deep theoretical (DFT or ab initio) analyses of their ground-state molecular orbitals (MO) and electronic absorption spectra with fully assigned electronic transitions. The only exceptions published to date are the group-7 metal complexes $[Mn(CO)_3(TMBP)]^-$(ref. [29]) and $[Re(CO)_3(BPY)]^-$ (ref. [34]). In a few other cases, simplified MO schemes and qualitative descriptions of the bonding situation have been published [15,18,24,42]. An illustrative MO scheme relevant to this article is depicted and analyzed in Fig. 1. In order to reduce the information gap, we present here a series of five-coordinate anionic complexes $[Mn(CO)_3(L_2)]^-$ with a variety of chelating π-donor ligands L_2 (Chart 1 and Fig. 2). According to the published experimental data, these complexes feature a dif-

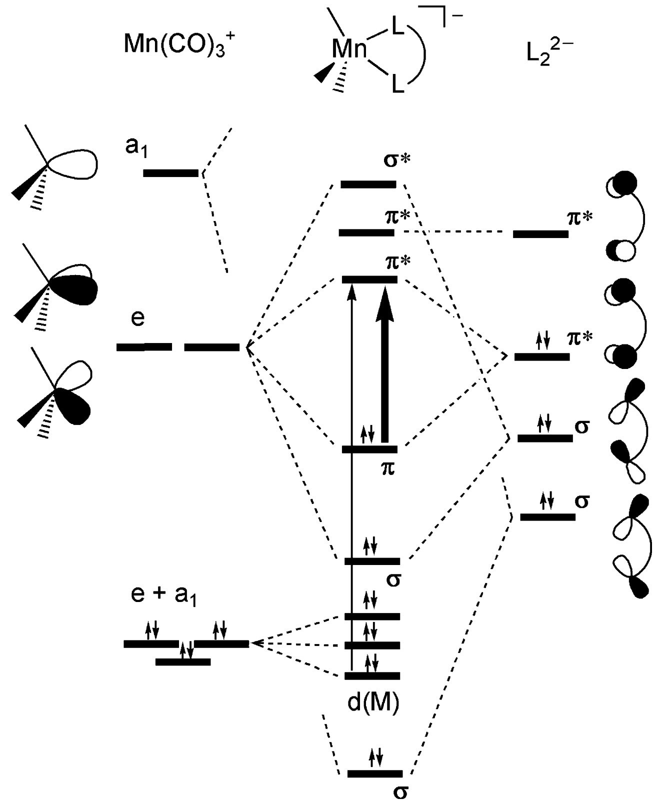

Fig. 1. Qualitative MO scheme for the five-coordinate complexes $[Mn(CO)_3(L_2)]^-$ being studied, adapted from the literature [18,24,42].

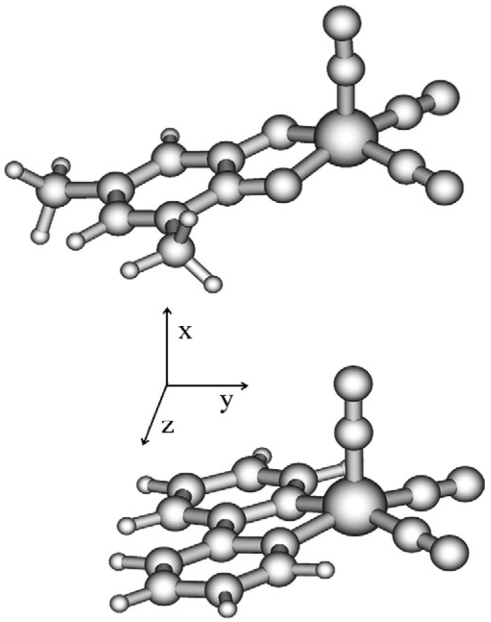

Fig. 2. Optimized B3LYP geometry of the complexes represented by $[Mn(CO)_3(Me\text{-}CAT)]^-$ (top) and $[Mn(CO)_3(BPY)]^-$ (bottom), together with the orientation of the cartesian coordinates used in the DFT calculations.

ferent degree of π-delocalization the Mn-L_2 chelate ring. We have selected the extended tricarbonyl manganese series as the far most representative and complete one, for every complex is well characterized in the literature. The only exception is $[Mn(CO)_3(BPY)]^-$, an important member of the series, where the synthesis, crystal structure and electronic absorption spectrum are published for the first time in this work. For comparison, we also deal with some representatives of the peculiar group of complexes [40,43]. $[Fe(CO)_3(R\text{-}DAB)]$ that may be isoelectronic with $[Mn(CO)_3(R\text{-}DAB)]^-$ (see above). The main goal is the thorough description of the electronic absorption spectra and the nature of the orbitals, excited states and electronic transitions involved. The bonding properties and reactivity of the complexes are also discussed to some extent, starting with the qualitative description in Fig. 1.

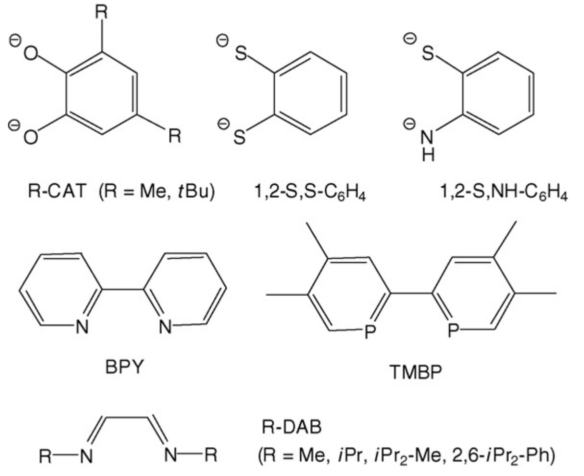

Chart 1. Chelating non-innocent ligands L_2^{2-} (in the uppermost row) and L_2 used in the investigated five-coordinate complexes $[Mn(CO)_3(L_2)^-$ and $[Fe(CO)_3(R\text{-}DAB)]$.

The frontier molecular orbitals of the trigonal pyramid $\{Mn(CO)_3\}^+$ moiety (C_{3v} symmetry) are combined with the right-symmetry counterparts of the formally two-electron reduced chelating ligand L_2. The occupied d(M) orbitals (M = Mn in this case) are not degenerate in the anionic complex having an idealized C_s symmetry. The unoccupied orthogonal e-orbitals of $\{Mn(CO)_3\}^+$ are involved in the σ- and π-bonding with L_2^{2-}; in fact, the free rotation of the chelated tricarbonyl fragment in solution [24] causes their interswitching. In the case of an aromatic L_2^{2-}, the empty π^* MO represents a low-lying orbital not involved in the strong π-bonding with the $\{Mn(CO)_3\}^+$ moiety. The strength of the π-interaction between $\{Mn(CO)_3\}^+$ and L_2^{2-}, controlled by their mutual energetic position, determines the extent of the π-donation from L_2^{2-} in $[Mn(CO)_3(L_2)]^-$ stabilizing the five-coordinate geometry of the complex. Representatives of the series with a low-lying $\pi^*(L_2^{2-})$ HOMO (e.g., catecholate complexes) and, hence, less π-delocalized bonding in the metallacycle, tend to uptake a sixth ligand, in particular at low temperature. In contrast, very stable five-coordination is achieved when the occupied $\pi^*(L_2^{2-})$ orbital rises in energy to approach the e_π level of $\{Mn(CO)_3\}^+$, as indicated by higher reduction potentials of neutral L_2 (e.g., going from an o-quinone to 2,2′-bipyridine). The e_π–$\pi^*(L_2^{2-})$ interaction weakens on going from Mn to Re, and the complexes $[Re(CO)_3(L_2)]^-$ are commonly six-coordinate. The main reason is the strongly labilized e-orbital set for the 5d metal. The larger ligand-field splitting of the metal-d orbital set for

Re causes also stabilization of the three occupied d(M) orbitals in the five-coordinate formally d^6 complex. Experimentally the splitting is consistent with a high-energy shift of the $d \rightarrow \pi^*$ electronic transition drawn as the thin arrow in Fig. 1, out of the visible spectroscopic region. As examples may serve the complexes $[M(CO)_3(i\text{Pr-DAB})]$ (M = Mn [28] and Re [30b]), and also the series $[M(\text{triphos})(t\text{Bu-CAT})]^+$ (M = Co, Rh, Ir) [42]. The thick arrows shows a low-energy electronic transition denoted as $\pi \rightarrow \pi^*$, which occurs between the frontier orbitals of the π-delocalized Mn–L_2 metallacycle and manifests itself usually as an intense absorption band in the visible spectroscopic region. This low-energy absorption is one of the characteristic features of the investigated class of five-coordinate electron-deficient complexes stabilized by strong π-donation from a simple non-innocent chelating ligand. The visible absorption spectra become more complicated and may be less easily interpreted using the above qualitative picture when other orbitals are involved in the optical excitation [34], such as a set of close-lying unoccupied π^* orbitals of aromatic chelating ligands represented here by BPY and TMBP (Chart 1).

2. DFT and TD-DFT calculations of electronically unsaturated complexes

2.1. $[Mn(CO)_3(R\text{-CAT})]^-$ (R-CAT = 3,5-di-R-1,2-O,O-C_6H_4; R = Me, tBu)

The ground-state bonding properties of the five-coordinate complex $[Mn(CO)_3(t\text{Bu-CAT})]^-$ (*t*Bu-CAT = 3,5-di-*tert*-butylcatecholate) were thoroughly investigated by a wealth of spectroscopic and electrochemical techniques [21–25].

The experimental results, especially the EPR spectrum of the one-electron-reduced metal-centered radical $[Mn^0(CO)_3(t\text{Bu-CAT})]^{2-}$ (a(Mn) = 5.34 mT, in THF), largely *t*Bu-CAT-based electrochemical oxidation, a nucleophilic attack of CS_2 at the *t*Bu-CAT oxygen atoms [25] and formation of six-coordinate adducts with Lewis bases at low temperatures, have pointed to a predominantly valence-localized, Mn^I-(*t*Bu-CAT) nature of the bonding. Some delocalization of the π HOMO and π^* LUMO (Fig. 1) over the Mn(*t*Bu-CAT) chelate ring and carbonyl ligands has been revealed by resonance Raman (rR) spectroscopy [24]. Light-excitation into the lowest-energy electronic transition of $[Mn(CO)_3(t\text{Bu-CAT})]^-$ at 546 nm had only a weak effect on the ν_s(CO) Raman band. On the other hand, it resulted in a significantly enhanced Raman band at 530 cm^{-1}, assigned tentatively to a Mn(*t*Bu-CAT) chelate-ring vibration. The lowest-energy $\pi \rightarrow \pi^*$ electronic transition within the Mn(*t*Bu-CAT) chelate ring (Fig. 1) has therefore a partial LMCT character. When the laser irradiation was directed into the higher-lying absorption band at 436 nm (see the inset to Fig. 4 below), the intensity of the ν_s(CO) Raman band increased considerably while that of the Raman band due to the chelate-ring vibrational mode decreased. In conformity with these changes, the corresponding electronic transition has been assigned [24] as $d(Mn) \rightarrow \pi^*$(LUMO), see Fig. 1. Despite the qualitatively correct bonding model used in the earlier publications [21,24,25], the present review benefits from the more accurate analysis based on the DFT MO calculations. The *t*Bu groups at the catecholate ligand have been replaced by methyl substituents in $[Mn(CO)_3(\text{Me-CAT})]^-$ to provide the best model for the experimentally studied *t*Bu-CAT complex.

Table 1
The comparison of selected experimental and DFT calculated bond lengths (Å) and angles (°) for $[Mn(CO)_3(\text{Me-CAT})]^-$ model complex

Bond(s)	ADF/BP	G03/B3LYP	Exp.[a]
Mn′—O′	1.939	1.921	1.916
Mn′—C1′$(CO)_{ap}$	1.793	1.796	1.727
Mn′—C′$(CO)_{bas}$	1.762	1.755	1.755
O4′—C4′	1.333	1.330	1.334
C4′—C5′	1.414	1.418	1.384
C′—C′$(Ph)_{av}$	1.406	1.402	1.391
C′—O′$(CO)_{av}$	1.175	1.167	1.174
Mn′—O′—C4′	113.4	113.5	–
O4′—Mn′—O5′	82.8	82.9	82.1
O′—Mn′—C1′$(CO)_{ap}$	108.0	106.2	111.0
O—Mn′—C′$(CO)_{bas}$	90.8	89.4	91.5

[a] Experimental (primed, square pyramidal) structure of $[Mn(CO)_3(t\text{Bu-CAT})]^-$ averaged in C_s symmetry [21].

Table 1 documents that both ADF/BP and G03/B3LYP data describe qualitatively well the experimental nearly square pyramidal geometry of one of the three independent $[Mn(CO)_3(t\text{Bu-CAT})]^-$ formula units contained within the asymmetric region of the unit cell. The optimized geometry of $[Mn(CO)_3(\text{Me-CAT})]^-$ was employed in the following single point electronic structure calculations.

In the previously reported [21,24] qualitative MO diagram of $[Mn(CO)_3(t\text{Bu-CAT})]^-$ (adapted in Fig. 1), the π HOMO of the complex is mainly localized on the *t*Bu-CAT ligand ($3b_1$ HOMO) and the lower-lying set of three occupied d(Mn) orbitals reside on the $\{Mn(CO)_3\}^+$ fragment. The π^* LUMO of the complex has been attributed a predominant $\{Mn(CO)_3\}^+$ character. The tricarbonyl metal fragment contributes here with one member of its lowest-lying empty e-orbital set, which is asymmetric with respect to the *t*Bu-CAT plane [44]. It follows that the π HOMO and π^* LUMO of $[Mn(CO)_3(t\text{Bu-CAT})^-$ are the bonding and antibonding combinations, respectively, with regard to the Mn–O bonds in the Mn(*t*Bu-CAT) chelate ring. Inspection of Table 2 reveals that these characters are largely reproduced in the DFT-calculated molecular orbitals 46a–50a, the LUMO and HOMO to HOMO − 3 of the model complex $[Mn(CO)_3(\text{Me-CAT})]^-$, respectively. The 49a HOMO is localized for 73% on the Me-CAT ligand while the 50a LUMO resides for 75% on the $\{Mn(CO)_3\}^+$ fragment (Fig. 3). The π delocalization within the Mn(Me-CAT) chelate ring is not negligible but still permits application of the valence-localized concept, in agreement with the experimental data briefly listed above. The 45a HOMO − 4 shows the predominant π (Me-CAT) contribution, while the 51a LUMO + 1 and 52a LUMO + 2, energetically well separated from the LUMO, reside again mainly on the $\{Mn(CO)_3\}^+$ fragment. We can deduce that the stabilizing catecholate-to-CO π-back-donation is directed mainly to the basal CO ligands. It is probably the apical CO ligand that becomes readily substituted by $P(OEt)_3$ to form the dicar-

Table 2
One-electron energies and percentage composition of selected highest occupied and lowest unoccupied molecular orbitals of $[Mn(CO)_3(Me\text{-}CAT)]^-$ expressed in terms of composing fragments.

MO	E (eV)	Mn	Me-CAT	CO_{ap}	CO_{bas}
Empty					
52a	2.31	1(p); 23(d)	18	6	51
51a	1.84	6(p); 36(d)	12	14	33
50a (π^*)[a]	0.62	10(p); 40(d)	25 (π^*)	9	16
Occupied					
49a (π)[a]	−1.18	5(p); 10(d)	73 (π^*)	1	10
48a	−1.68	2(p); 41(d)	34 (π)	13	9
47a	−1.82	58(d)	16	1	24
46a	−2.09	2(p); 51(d)	19	14	13
45a	−2.32	16(d)	78 (π)	4	1

[a] The π and π^* notation of the frontier orbitals refers to the Mn(Me-CAT) chelate ring.

bonyl derivative $[Mn\{P(OEt)_3\}(CO)_2(t\text{Bu-CAT})]^-$ with bonding, redox and spectroscopic properties similar to those of the parent tricarbonyl anion [24,25].

The G03/B3LYP-computed electronic absorption spectrum of $[Mn(CO)_3(Me\text{-}CAT)]^-$ (Fig. 4) reproduces reasonably well the experimental spectrum of $[Mn(CO)_3(t\text{Bu-CAT})]^-$ (Fig. 4, inset). Curiously, the intensity pattern of the two main absorption bands in the visible region resembles more closely that of $[Mn\{P(OEt)_3\}(CO)_2(t\text{Bu-CAT})]^-$ [24]. The intensity ratio is better reproduced by ADF/BP; although, this method gives a slightly larger deviation of the calculated transition energies from the experimental values (Table 3).

According to the TD-DFT data, the absorption band of $[Mn(CO)_3(t\text{Bu-CAT})]^-$ at 2.28 eV (546 nm) corresponds to a mixed electronic transition with a significant 49a HOMO → 50a LUMO component. The predominant LMCT (catecholate → Mn(CO)) character of the lowest optically available excited state is reflected in the resonance Raman (rR) spectrum of $[Mn(CO)_3(t\text{Bu-CAT})]^-$ (ref. [24]), which shows enhanced intensity of several Raman bands between 1200 and 1550 cm^{-1} belonging to coupled ν(C–O) and ν(C–C) skeletal vibrations of the catecholate ring. On the other hand, the considerable delocalization of the frontier orbitals of $[Mn(CO)_3(t\text{Bu-CAT})]^-$ (denoted as π and π^*(Mn-CAT)) over the Mn(tBu-CAT) chelate ring and the three carbonyl ligands (see Fig. 3 and Table 2 for the Me-CAT model) results in a strong resonant enhancement of a Raman band at 530 cm^{-1}. The latter band is attributed to a deformation of the square pyramidal coordination geometry around the Mn center upon the predominant 49a → 50a ($\pi \rightarrow \pi^*$) excitation (Tables 3 and 4). The appearance of the ν(Mn–O) peak at 611 cm^{-1} in the rR spectrum also documents the involvement of the Mn(tBu-CAT) chelate ring in the $\pi \rightarrow \pi^*$ electronic transition.

The higher-lying absorption band of $[Mn(CO)_3(t\text{Bu-CAT})]^-$ at 2.89 eV (436 nm) does not correspond to a simple d(Mn) → π^*(Mn-tBu-CAT) electronic transition, as was proposed elsewhere [24]. Instead, it originates from several low-lying occupied orbitals of a mixed Mn (d), catecholate (π^* and π) and carbonyl nature. These contributing excitations are directed mainly to the lowest empty π^*(Mn-tBu-CAT) orbital. Therefore, this absorption band cannot be assigned to any specific type of electronic transition (MC, IL, MLCT). The strong participation of the d(Mn) orbitals involved in the Mn → CO π-back-bonding is probably responsible for a large intensity enhancement of the high-frequency ν(C≡O) Raman band, which becomes strongly diminished upon the lowest-energy $\pi \rightarrow \pi^*$ optical excitation within the Mn(tBu-CAT) moiety.

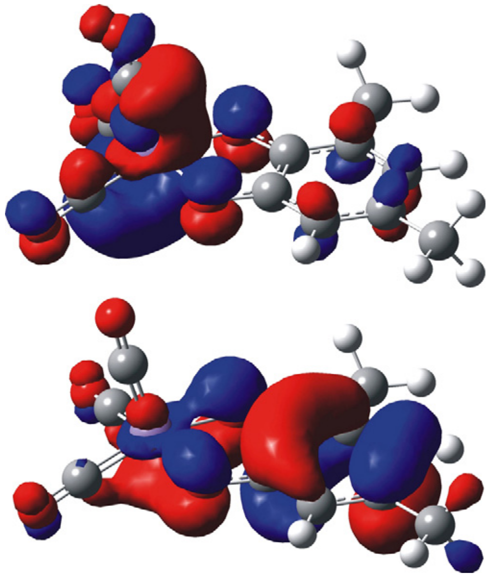

Fig. 3. Representation of the HOMO (bottom) and LUMO (top) of $[Mn(Me\text{-}CAT)(CO)_3]^-$.

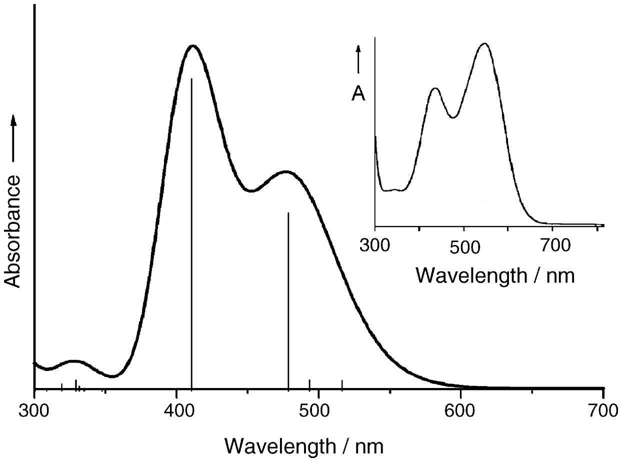

Fig. 4. The simulated electronic absorption spectrum of $[Mn(CO)_3(Me\text{-}CAT)]^-$ based on G03/B3LYP calculated excitation energies and oscillator strengths (represented by vertical lines). Inset: The experimental electronic absorption spectrum of $[Mn(CO)_3(t\text{Bu-CAT})]^-$ in THF at 293 K.

2.2. $[Mn(CO)_3(R\text{-}DAB)]^-$ (R-DAB = 1,4-di-R-1,4-diazabutadiene; R = Me, iPr) and $[Fe(CO)_3(R\text{-}DAB)]$ (R = Me, iPr_2-Me, 2,6-iPr_2-Ph)

The calculated geometry of the five-coordinate complex $[Fe(CO)_3(Me\text{-}DAB)]$ is in very good agreement with the experimental distorted square pyramidal structure reported [43] for

Table 3
Selected TD-DFT calculated lowest-lying singlet excitation energies for [Mn(CO)$_3$(Me-CAT)]$^-$ with oscillator strength (O.S.) larger than 0.005

State	Composition (ADF/BP)	ADF/BP		G03/B3LYP		Experiment	
		Transition energy (eV)	O.S.	Transition energy (eV)	O.S.	Transition energy (eV)	ε_{max} (M^{-1} cm^{-1})
c^{1}A	62% (49a → 50a) 25% (47a → 50a)	2.66	0.132	2.59	0.091	2.28	8300
d^{1}A	70% (47a → 50a) 16% (49a → 50a)	2.71	0.043				
e^{1}A	50% (49a → 51a) 29% (46a → 50a)	3.12	0.017	3.02	0.160	2.89	6900
f^{1}A	41% (45a → 50a) 39% (46a → 50a) 7% (49a → 50a)	3.19	0.051				

Table 4
Selected DFT G03/BPW91 calculated Raman-active frequencies for [Mn(CO)$_3$(tBu-CAT)]$^-$

ν (cm^{-1})	ν (cm^{-1})[a]	Assignment
519	530	δ(C–Mn–C) + δ(O–Mn–O)
569, 586	580	δ(C–Mn–C) + δ(O–Mn–O)
613	611	ν(Mn–O)
1273	1254	ν(C–O) (CAT)
1308	1316	ν(C–O) + ν(C–C) (CAT)
1423	1410	ν(C–O) + ν(C–C) (CAT)
1446	1434	ν(C–C) (CAT)
1474	1463	ν(C–C) (CAT) + δ(CH)
1541	1551	ν(C–C) (CAT)

[a] Experimental resonance Raman spectrum [24].

the derivative with the 2,6-iPr$_2$-Ph-DAB ligand (Table 5). Crystallographic data for a complex anion [Mn(CO)$_3$(R-DAB)]$^-$ were not available. The structural parameters calculated by both DFT methods for the model compound [Mn(CO)$_3$(Me-DAB)]$^-$ closely resemble those of the neutral Fe complex. We therefore do not expect significant differences between the molecular structures of the two species. The slightly longer C≡O bonds and shorter M—CO bonds in [Mn(CO)$_3$(Me-DAB)]$^-$ compared to [Fe(CO)$_3$(Me-DAB)] (Table 5) indicate a stronger Mn → CO π-back-donation in the negatively charged complex. A comparison of [Mn(CO)$_3$(Me-DAB)]$^-$ with [Mn(CO)$_3$(Me-CAT)]$^-$ (Table 1) shows even smaller differences between these parameters and does not allow any conclusive statement about the extent of π-delocalization of the Mn–L$_2$ bonding. More revealing in this regard are the experimental IR ν(CO) frequencies. The much lower values for [Mn(CO)$_3$(iPr-DAB)]$^-$ (1919 and 1811(br) cm^{-1} in butyronitrile) [28] compared to [Mn(CO)$_3$(tBu-CAT)]$^-$ (1994 and 1891(br) cm^{-1} in THF) [24] point to a fully delocalized π-bonding within the Mn(NCCN) metallacycle. This situation is in line with the lack of ability of the five-coordinate anion [Mn(CO)$_3$(iPr-DAB)]$^-$ to undergo adduct formation or CO-substitution reactions in the presence of Lewis bases.

The DFT calculated composition of the highest occupied and lowest unoccupied molecular orbitals of [Mn(CO)$_3$(Me-DAB)]$^-$ is presented in Table 6. The 24a′HOMO and 25a′LUMO, shown in Fig. 5, are indeed strongly delocalized over the Me-DAB ligand and the {Mn(CO)$_3$} moiety. The π* LUMO of Me-DAB contributes slightly more to the HOMO of the complex, while the LUMO of the complex resides more on the Mn center and the carbonyl ligands. The higher-lying empty orbitals (17a″ LUMO + 1 and 26a′ LUMO + 2) are localized considerably more on the carbonyl ligands. The lower-lying occupied orbitals (HOMO − 1 to HOMO − 3) are mainly com-

Table 5
DFT calculated bond lengths (Å) and angles in [M(CO)$_3$(Me-DAB)]^n (n = 0 for M = Fe and n = −1 for M = Mn) model complexes

Bond(s)	M = Fe ADF/BP	G03/B3LYP	Exp.[a]	M = Mn ADF/BP	G03/B3LYP
M—N	1.934	1.931	1.927	1.963	1.960
M—C(CO)$_{ap}$	1.780	1.793	1.800	1.786	1.785
M—C(CO)$_{bas}$	1.778	1.773	1.788	1.769	1.749
N—C	1.336	1.331	1.329	1.354	1.364
C4—C5	1.397	1.392	1.390	1.381	1.371
N—C(Me)	1.464	1.462	1.442	1.454	1.454
C—O(CO)$_{av}$	1.164	1.147	1.143	1.183	1.174
N—M—N′	80.6	81.0	80.1	79.3	79.9
M—N—C	115.2	114.6	115.4	115.7	115.1
N—C—C′	114.4	114.8	114.2	114.5	114.8
N—M—C(CO)$_{ap}$	103.9	102.0	106.3	105.9	105.6
N—M—C(CO)$_{bas}$	91.1	90.3	91.0	91.1	91.0

[a] Experimental structure of [Fe(CO)$_3$(R-DAB)] (R = 2,6-diisopropyl-phenyl) averaged in C_s symmetry [43].

Table 6
One-electron energies and percentage composition of selected highest occupied and lowest unoccupied molecular orbitals of $[Mn(CO)_3(Me\text{-}DAB)]^-$ expressed in terms of composing fragments

MO	*E* (eV)	Mn	Me-DAB	CO_{ap}	CO_{bas}
Empty	–				
26a′	3.35	$16(d_{z^2}); 10(d_{x^2-y^2})$	6	5	61
17a″	2.99	$6(p_z); 24(d_{xz})$	16	16	38
25a′	1.91	$7(p_x); 2(d_{z^2}); 6(d_{x^2-y^2}); 21(d_{xy})$	$42\,(\pi^*)$	10	12
Occupied					
24a′	0.01	$10(p_x); 7(d_{z^2}); 8(d_{x^2-y^2}); 4(d_{xy})$	$55\,(\pi^*)$	2	14
16a″	−0.69	$3(p_z); 52(d_{xz}); 2(d_{yz})$	$13\,(\pi)$	17	12
23a′	−0.99	$1(p_y); 29(d_{z^2}); 1(d_{x^2-y^2}); 32(d_{xy})$	8	7	20
22a′	−1.10	$3(p_y); 22(d_{z^2}); 32(d_{x^2-y^2}); 8(d_{xy})$	2	9	23
15a″	−2.43	$6(d_{xz})$	$89\,(\pi)$	3	2

binations of the d(Mn) orbitals with small p-orbital components and significant contributions from the carbonyl ligands. An occupied π orbital of the Me-DAB ligand dominates the 15a″ HOMO − 4. With the exception of the strongly delocalized HOMO and LUMO, the characters of the higher and lower-lying molecular orbitals closely resemble those of $[Mn(CO)_3(Me\text{-}CAT)]^-$ (Table 2). We can therefore state that the distribution of the negative charge in these two five-coordinate complexes corresponds fairly well with their HOMO characters. Starting with the hypothetic two-electron-oxidized (16e) $\{(CO)_3Mn^I\text{-}L_2\}^+$ moiety, the added two electrons mainly reside at L_2 in the case of $L_2 = o$-quinone, i.e., giving rise to the largely valence-trapped $\{(CO)_3Mn^I\}^+\text{–}{L_2}^{2-}$ = catecholate bonding stabilized significantly, but not completely, by the catecholate → Mn(CO) π-donation. On the other hand, the two-electron reduction of $\{(CO)_3Mn^I\text{–R-DAB}\}^+$ (R = alkyl) results in almost completely delocalized $\{(CO)_3Mn\text{–R-DAB}\}^-$ charge distribution in the stable five-coordinate anion, with a strong Mn → CO π-back-bonding and highly problematic assignment of the formal oxidation state of the Mn center. Using the formal oxidation states Mn(0) and R-DAB$^-$ would imply a low-spin d^7 (Mn) configuration and a radical-anionic chelating ligand. In such a case, a strong antiferromagnetic coupling between the unpaired Mn and DAB electrons would explain the apparent diamagnetism of the complex. We refrain from this description.

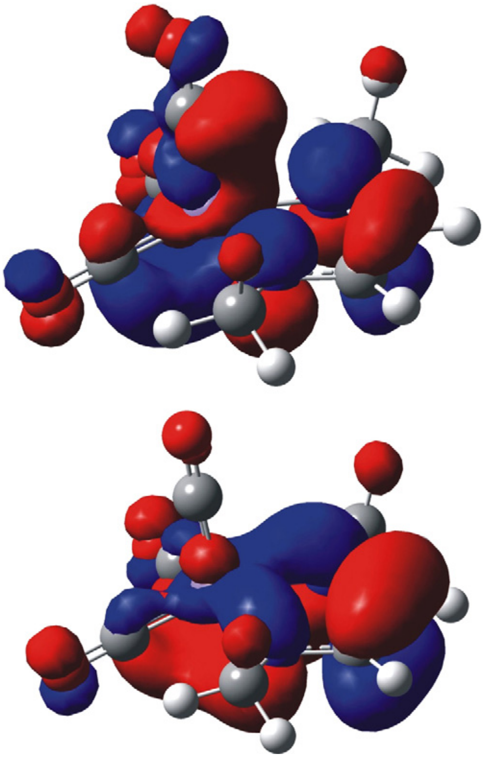

Fig. 5. The representations of the HOMO (bottom) and LUMO (top) of $[Mn(CO)_3(Me\text{-}DAB)]^-$.

Similar to the $[Mn(CO)_3(t\text{Bu-CAT})]^-$ complex in the preceding section, the UV–vis spectrum of $[Mn(CO)_3(i\text{Pr-DAB})]^-$ shows two dominant absorption bands in the visible region (Fig. 7 and Table 7). The TD-DFT data calculated for the model anion $[Mn(CO)_3(Me\text{-}DAB)]^-$ (Table 7) reproduce perfectly the experimental parameters. In the simulated electronic absorption spectrum (Fig. 6), the lowest-lying absorption band mainly corresponds to optical excitation into the strongly delocalized 24a′ HOMO → 25a′ LUMO transition ($\pi(Mn\text{–}L_2) \rightarrow \pi^*(Mn\text{–}L_2)$ in Fig. 1). Its limited R-DAB → Mn(CO) charge-transfer (LMCT) character is compensated by a partial mixing with the 23a′ HOMO − 2 → 25a′ LUMO (i.e., MLCT) transition.

The fully delocalized nature and negligible charge-transfer character of the lowest-energy $\pi(Mn\text{–}L_2) \rightarrow \pi^*(Mn\text{–}L_2)$ transition (in line with the lack of solvatochromism) are also clearly reflected in the experimental resonance Raman spectrum of $[Mn(CO)_3(i\text{Pr-DAB})]^-$ recorded within a thin-layer optically transparent electrochemical (OTTLE) cell in order to exclude air and moisture. Electronic excitation with the 514.5-nm argon-ion laser line resulted in the appearance of Raman bands listed in Table 8. The resonance Raman effect for this five-coordinate complex is weak, which means that the geometry and bond lengths of the complex hardly change upon excitation. The strongest enhancement of the Raman intensity was observed for the band at 839 cm^{-1}, which corresponds to mixed bending modes of the Mn(*i*Pr-DAB) chelate ring. According to the DFT calculated wavenumbers and characters in Table 8, also the other Raman modes belong to deformation of the five-coordinate anion. Importantly, no band was observed in the

Table 7
Selected TD-DFT calculated lowest-lying singlet excitation energies (eV) for $[Mn(CO)_3(Me\text{-}DAB)]^-$ with oscillator strength (O.S.) larger than 0.005

State	Composition (ADF/BP)	ADF/BP		G03/B3LYP		Experiment	
		Transition energy (eV)	O.S.	Transition energy (eV)	O.S.	Transition energy (eV)	ε_{max} (M^{-1} cm^{-1})
b^1A'	79% ($24a' \rightarrow 25a'$) 16% ($23a' \rightarrow 25a'$)	2.74	0.083	2.68	0.091	2.55	9300
a^1A''	83% ($16a'' \rightarrow 25a'$) 15% ($21a' \rightarrow 17a''$)	3.14	0.005	2.68	0.006		
d^1A'	66% ($23a' \rightarrow 25a'$) 10% ($22a' \rightarrow 25a'$) 14% ($24a' \rightarrow 25a'$)	3.36	0.065	3.24	0.073	3.21	6550
$^1A'$	78% ($24a' \rightarrow 29a'$)	4.14	0.012	4.30	0.018		

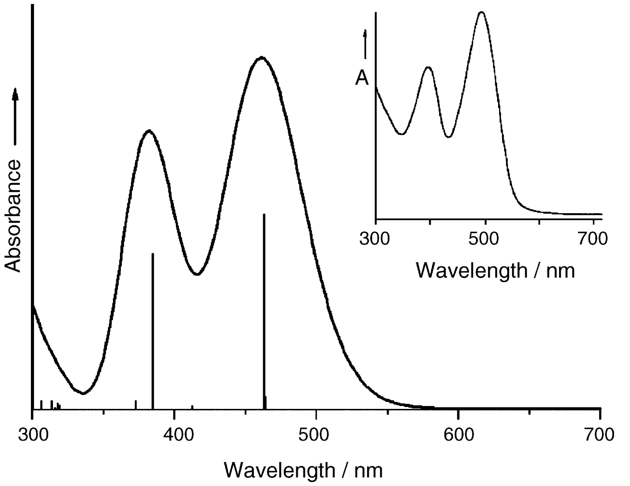

Fig. 6. The simulated electronic absorption spectrum of $[Mn(CO)_3(Me\text{-}DAB)]^-$ based on G03/B3LYP calculated excitation energies and oscillator strengths (represented by vertical lines). *Inset*: The experimental electronic absorption spectrum of $[Mn(CO)_3(i\text{Pr-DAB})]^-$ in MeCN/10^{-1} M Bu_4NPF_6 at 293 K.

CO-stretching region of the rR spectrum, as expected for the almost unaffected Mn → CO π-back-donation in the $\pi \rightarrow \pi^*$ (Mn(*i*Pr-DAB)) excited state compared to the ground state.

The higher-lying intense absorption band has apparently a complicated character, with a dominant HOMO − 2 → LUMO contribution that can be simplified as $d(Mn) \rightarrow \pi^*(L_2)$ (i.e., MLCT) optical excitation, in line with Fig. 1. Evidently, the latter electronic transition has a more pronounced charge-transfer character than the lowest-energy one.

Table 8
Selected DFT G03/BPW91 calculated Raman-active frequencies for $[Mn(CO)_3(i\text{Pr-DAB})]^-$

ν (cm^{-1})	ν (cm^{-1})[a]	Assignment
531	517	δ(C–Mn–C) + δ(N–Mn–N)
820	839	δ(*i*Pr-DAB) + δ(N–Mn–N)
901	893	δ(*i*Pr-DAB)
924	917	δ(*i*Pr-DAB)
1216	1251	ν(CN) + δ(CH) (a″)
1255	1294	ν(CN) + δ(CH) (a″)
1328	1328	δ(CH)

[a] Experimental data [45].

Molecular orbitals of the neutral complex $[Fe(CO)_3(Me\text{-}DAB)]$ are presented in Table 9. The qualitative MO scheme calculated for this complex is similar to that of the anion $[Mn(CO)_3(Me\text{-}DAB)]^-$ (Table 6). The main difference concerns the frontier orbitals. The 24a′ HOMO is more localized on the $\{Fe(CO)_3\}$ fragment while the 25a′ LUMO resides more on the Me-DAB ligand. The characters of the LUMO + 2, LUMO + 1 and HOMO − 1 to HOMO − 4 of the two five-coordinate Me-DAB species are comparable. Taking into account the highly delocalized nature of the frontier orbitals (Fig. 7), we can better describe the bonding situation in the $[Fe(CO)_3(R\text{-}DAB)]$ complexes formally as $\{Fe(CO)_3\}^{\delta+}$–R-DAB$^{\delta-}$, i.e., with some π-donation from R-DAB to the electron-deficient $\{Fe(CO)_3\}$ fragment, rather than $Fe(CO)_3$–R-DAB (18e). The former representation is supported by the relatively high ν(CO) frequencies of $[Fe(CO)_3(R\text{-}DAB)]$ (2041, 1973 and 1967 cm^{-1} for the 2,6-*i*Pr_2-Ph-DAB ligand, and 2026, 1955 and 1946 cm^{-1} for the *i*Pr_2-Me-DAB ligand) [43] in comparison, for example, with the values for the complexes $[Fe(CO)_3(PP)]$ (PP = chelating biphosphine ligand). $[Fe(CO)_3(dmpe)]$ (dmpe = dimethylphosphinoethane) absorbs in THF at 1976, 1902 and 1887 cm^{-1} [46]. On the other hand, the complex $[Fe(CO)_3Cp]$ ($Cp = \eta^5\text{-}C_5H_5$), which can also be denoted as $\{Fe(CO)_3\}^{\delta+}$–$Cp^{\delta-}$, shows comparable ν(CO) frequencies as $[Fe(CO)_3(R\text{-}DAB)]$, viz. 2048, 1981 and 1974 cm^{-1} [47].

Taking into account the similar nature and energies of the high-lying occupied and low-lying empty molecular orbitals of $[Mn(CO)_3(R\text{-}DAB)]^-$ and $[Fe(CO)_3(R\text{-}DAB)]$, it is not surprising that their electronic absorption spectra are also very similar. $[Fe(CO)_3(i\text{Pr}_2\text{-Me-DAB})]$ again shows, in the visible region, (Table 10) two main absorption bands that are perfectly reproduced in the computed spectrum of the model $[Fe(CO)_3(Me\text{-}DAB)]$. A similar UV–vis spectrum has been reported also for the iron tricarbonyl complex with the 2,6-*i*Pr_2-Ph-DAB ligand [43]. Apparently, the different nature of the substituents at the imine nitrogen atoms of the R-DAB ligands does not play a significant role in this case. The lowest-energy electronic transition consists mainly of the 24a′ → 25a′ (HOMO → LUMO) excitation. Differently from $[Mn(CO)_3(Me\text{-}DAB)]^-$, this electronic transition has a partial MLCT character. This difference may account for the reported efficient photosubstitution of a

Table 9
One-electron energies and percentage composition of selected highest occupied and lowest unoccupied molecular orbitals of $[Fe(CO)_3(Me\text{-}DAB)]$ expressed in terms of composing fragments

MO	E (eV)	Fe	Me-DAB	CO_{ap}	CO_{bas}
Empty					
26a′	−1.61	$12(d_{z^2})$; $5(d_{x^2-y^2})$	3	3	74
17a″	−2.07	$4(p_z)$; $45(d_{xz})$	22	8	21
25a′	−2.97	$3(p_x)$; $2(d_{z^2})$; $6(d_{x^2-y^2})$; $15(d_{xy})$	$61(\pi^*)$	5	6
Occupied					
24a′	−4.81	$12(p_x)$; $9(d_{z^2})$; $15(d_{x^2-y^2})$; $8(d_{xy})$	$39(\pi^*)$	3	15
16a″	−5.72	$3(p_z)$; $55(d_{xz})$; $2(d_{yz})$	$19(\pi)$	12	8
23a′	−6.12	$4(p_y)$; $2(d_{z^2})$; $13(d_{x^2-y^2})$; $47(d_{xy})$	9	9	13
22a′	−6.36	$1(p_y)$; $56(d_{z^2})$; $19(d_{x^2-y^2})$; $1(d_{xy})$	2	1	20
15a″	−7.17	$10(d_{xz})$	$84(\pi)$	3	2

CO ligand in $[Fe(CO)_3(2,6\text{-}i\text{Pr}_2\text{-Ph-DAB})]$ by PPh_3 (although probably not from the initially populated excited state) [48], while the more π-delocalized complex $[Mn(CO)_3(i\text{Pr-DAB})]^-$ is photostable. On the other hand, the resonance Raman spectra of $[Fe(CO)_3(2,6\text{-}i\text{Pr}_2\text{-Ph-DAB})]$ recorded upon irradiation into the lowest-energy absorption band [43], show only weak effects for the ν_s(CO) and DAB ν(CN) modes, but strong resonance enhancement of Raman intensities for bands corresponding to low-frequency ν(Fe–C), δ(Fe–CO) and δ(Fe–DAB) modes. This result and the absence of solvatochromism are in favor of a strongly delocalized nature of the lowest-energy excited state. The previous analysis of the Raman excitation profiles by Stufkens et al., invoked the presence of three independent close-lying electronic transitions within the lowest-energy absorption band of $[Fe(CO)_3(2,6\text{-}i\text{Pr}_2\text{-Ph-DAB})]$ [43]. This feature is, however, not reproduced in our TD-DFT calculations (Table 10).

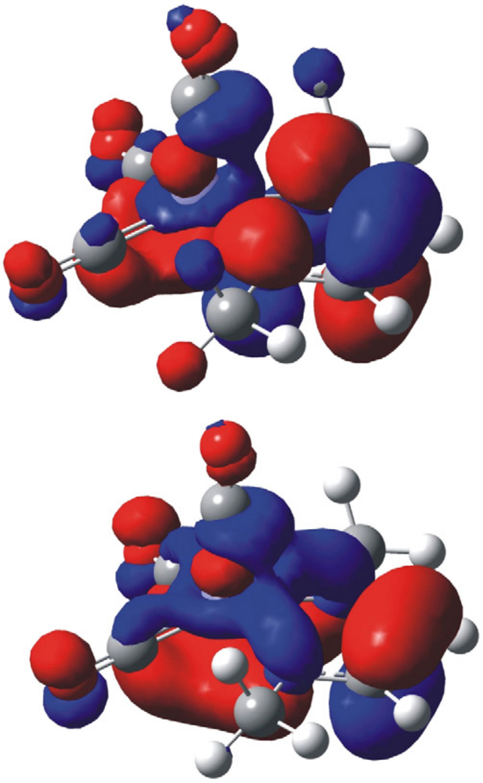

Fig. 7. The representation of the HOMO (bottom) and LUMO (top) of $[Fe(Me\text{-}DAB)(CO)_3]$.

Similar to $[Mn(CO)_3(Me\text{-}DAB)]^-$, the higher-lying absorption band in the UV–vis spectrum of the iron complex has its origin in a strongly mixed electronic transition between the ground-state Kohn-Sham molecular orbitals, with the principal 23a′ HOMO − 2 → 25a′ LUMO component. This transition has an apparent MLCT (d → π*) character, which agrees with the increasing intensity of the Raman bands due to the ν_s(CO) and intraligand ν(CN) modes in the resonance Raman spectra of $[Fe(CO)_3(2,6\text{-}i\text{Pr}_2\text{-Ph-DAB})]$ [43].

2.3. $[Mn(CO)_3(BPY)]^-$ (BPY = 2,2′-bipyridine)

The extremely air- and moisture-sensitive anion $[Mn(CO)_3(BPY)]^-$ was prepared under strictly inert conditions by reduction of $[MnBr(CO)_3(BPY)]$ with sodium naphthalenide. The product could be crystallized from diethyl ether in a sealed tube to give an unusual structure, $[Na(BPY)][Mn(CO)_3(BPY)]\cdot Et_2O$, with tetrahedral coordination of the sodium counterion linked to one of the CO ligands and one diethyl eiher molecule (Scheme 1, Fig. 8, Table 11). The BPY ligand

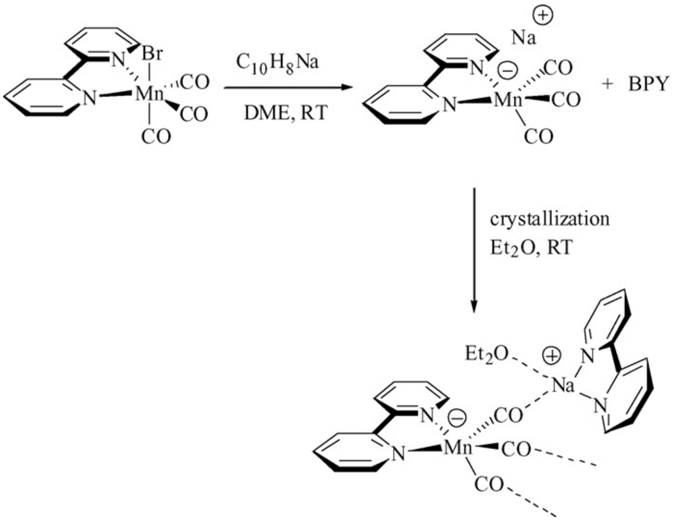

Scheme 1.

Table 10
Selected TD-DFT calculated lowest-lying singlet excitation energies (eV) for [Fe(CO)$_3$(Me-DAB)] with oscillator strength (O.S.) larger than 0.001

State	Composition (ADF/BP)	ADF/BP		G03/B3LYP		Exp.[a]	
		Transition energy (eV)	O.S.	Transition energy (eV)	O.S.	Transition energy (eV)	ε_{max} (M^{-1} cm^{-1})
b^{1}A′	78% (24a′ → 25a′) 17% (23a′ → 25a′)	2.73	0.076	2.56	0.083	2.49	5900
a^{1}A″	83% (16a″ → 25a′) 15% (24a′ → 17a″)	2.93	0.005	2.79	0.002		
d^{1}A′	40% (23a′ → 25a′) 27% (22a′ → 25a′) 19% (24a′ → 26a′)	3.48	0.043	3.29	0.055	3.33	3000
e^{1}A′	51% (22a′ → 25a′) 30% (23a′ → 25a′) 6% (24a′ → 26a′)	3.61	0.028	3.59	0.031	3.98	sh

[a] For [Fe(CO)$_3$(*i*Pr$_2$-Me-DAB)] in benzene at 293 K [43].

attached to the sodium cation probably liberated by a partial decomposition of the complex anion prior to the crystallization. The Mn center adopted a geometry that can be best described as a transition between a distorted square pyramid and trigonal bipyramid. Comparison of the two different BPY ligands reveals significant shortening of the inter-ring C–C bond in the Mn-bound BPY (1.418(3) Å versus 1.491(3) Å for the Na-bound BPY). The Mn-bound BPY shows intra-ring bond lengths alternating between 1.36 and 1.41 Å, in contrast to the regular C–C distances (1.38–1.39 Å) in the Na-bound BPY. The latter ligand strongly resembles BPY in the non-reduced complex [MnI(CO)$_3$(BPY)] (ref. [49]) (Table 12). These data are consistent with a substantial localization of electron density in the π* LUMO of the Mn-bound BPY ligand and

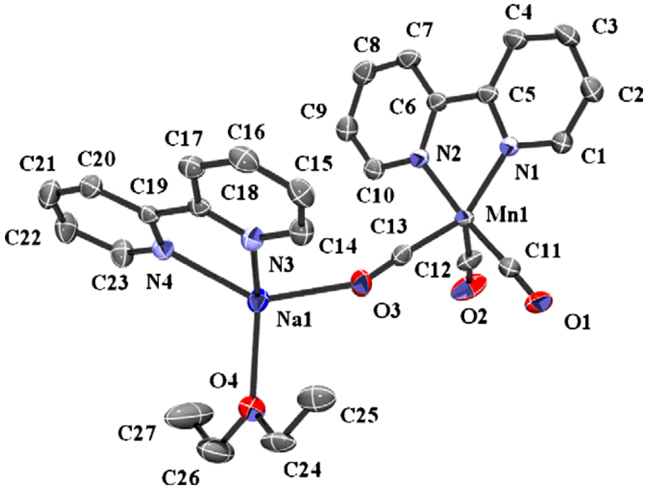

Fig. 8. ORTEP view of one molecule of [Na(BPY)][Mn(CO)$_3$(BPY)]·Et$_2$O. Ellipsoids are scaled to enclose 50% of the electron density. The numbering is arbitrary and different from that used in the assignment of NMR spectra. Relevant distances (Å) and bond angles (°): N1–C1, 1.375(3); C1–C2, 1.364(4); C2–C3, 1.413(4); C3–C4, 1.364(4); C4–C5, 1.414(3); C5–N1, 1.391(3); C5–C6, 1.418(3); C6–C7, 1.411(3); C6–N2, 1.378(3); C7–C8, 1.366(4); C8–C9, 1.408(4); C9–C10, 1.362(3); C10–N2, 1.370(3); N1–Mn1, 1.980(2); N2–Mn1, 1.981(2); Mn1–C11, 1.771(2); Mn1–C12, 1.796(3); Mn1–C13, 1.767(2); C11–O1, 1.176(3); C12–O2, 1.157(3); C13–O3, 1.172(3); Na1–O3, 2.334(2); N3–Na1, 2.430(2); N4–Na1, 2.417(2); N3–C14, 1.339(3); N3–C18, 1.349(3); C18–C19, 1.491(3); C19–N4, 1.347(3); N1–Mn1–N2, 78.79(8); C13–Mn1–C11, 87.4(1); C13–Mn1–C12, 96.7(1); C11–Mn1–C12, 93.8(1); Mn1–C11–O1, 177.4(2); Mn1–C12–O2, 175.1(3); Mn1–C13–O3,176.0(2); N3–Na1–N4, 67.58(7).

Table 11
Crystal data for the structure of [Na(BPY)][Mn(CO)$_3$(BPY)]·Et$_2$O

Molecular formula	$C_{27}H_{26}MnN_4NaO_4$
Molecular weight	548.45
Crystal habit	Dark red plate
Crystal dimensions (mm)	0.20 × 0.20 × 0.17
Crystal system	Monoclinic
Space group	$P2_1c$
a (Å)	10.7836(3)
b (Å)	18.4574(6)
c (Å)	13.8223(3)
α (°)	90.00
β (°)	102.815(2)
γ (°)	90.00
V (Å^3)	2682.62(13)
Z	4
d (g cm^3)	1.358
F(0 0 0)	1136
μ (cm^{-1})	0.547
Diffractometer	Kappa CCD
X-ray source	Mo Kα
T (K)	150.0(1)
Scan mode	Phi and omega scans
Maximum θ	27.47
hkl ranges	−13, 12; −22, 23; −17, 15
Reflections measured	16365
Unique data	6116
R_{int}	0.0494
Reflections used	5254
Criterion	$I > 2\sigma I$
Parameters refined	380
Reflections/parameter	13
$wR2$	0.1197
$R1$	0.0447
Weights a, b	0.0331; 2.8913
GoF	1.125
Difference peak/hole (e Å^{-3})	0.437(0.064)/−0.335(0.064)

Table 12
Comparison of selected experimental and DFT-calculated bond lengths (Å) and angles in $[Mn(CO)_3(BPY)]^-$, and experimental bond lengths of $[MnI(CO)_3(BPY)]$

Bond(s)	ADF/BP	G03/B3LYP	Exp.[a]	Exp.[b]
Mn–N	1.986	1.980	1.981	2.04
Mn–C12(CO)$_{ap}$	1.789	1.784	1.796	1.80
Mn–C(CO)$_{bas}$	1.774	1.753	1.769	1.79
N1–C1	1.371	1.372	1.373	1.34
N1–C5	1.403	1.402	1.385	1.36
C1–C2	1.375	1.370	1.363	1.39
C2–C3	1.424	1.426	1.410	1.38
C3–C4	1.378	1.372	1.365	1.37
C4–C5	1.415	1.420	1.412	1.39
C5–C6	1.419	1.410	1.418	1.48
C–O(CO)$_{av}$	1.183	1.172	1.168	1.16
N1–Mn–N2	79.2	79.3	78.8	
Mn–N1-C1	126.8	126.9	127.2	
Mn–N1–C5	116.6	116.7	117.0	
N1–C5–C6	113.4	113.5	113.4	
N1–C5–C4	120.9	120.9	121.5	
C1–N1–C5	116.4	116.2	115.9	
N1–C1–C2	124.4	124.7	124.3	
C1–C2–C3	119.2	119.2	119.5	
C2–C3–C4	117.8	118.0	118.3	
N1–Mn–C11	93.4	92.8	93.5	
C11–Mn–C12	87.6	88.9	93.8	

[a] Experimental structure of $[Na(BPY)][Mn(CO)_3(BPY)]\cdot Et_2O$ averaged in C_s symmetry.

[b] Selected (averaged) bond lengths in the experimental structure of $[MnI(CO)_3(BPY)]$ [49].

the formulation of $[Mn(CO)_3(BPY)]^-$ as a compound with fully delocalized π-bonding in the Mn(BPY) metallacycle and strong (BPY)Mn → CO π-back-donation. This description is supported by the low IR CO-stretching frequencies: 1916(s) and 1815(s,br) cm^{-1} (for the Bu_4N^+ salt in PrCN) [27] compared to the values for valence-trapped $[Mn(CO)_3(t\text{Bu-CAT})]^-$ (see above). We conclude that the bonding situation in both anionic α-diimine complexes $[Mn(CO)_3(L_2)]^-$ (L_2 = BPY and *i*Pr-DAB in Section 2.2) is very similar. However, their electronic absorption spectra are considerably different (Figs. 6 (inset) and 10 (inset)). Based on the TD-DFT calculations, we have been able to clarify this difference by the involvement of several closely lying unoccupied, largely π*(BPY)-based molecular orbitals in the low-energy electronic transitions, see below.

The experimental and DFT-computed bonding parameters of $[Mn(CO)_3(BPY)]^-$ are again in a very good agreement (Table 12). The optimized geometry was employed in the following single point electronic structure calculations. Calculated energies and compositions of Kohn-Sham molecular orbitals of the anionic complex are collected in Table 13. The frontier orbitals have very similar, strongly (CO)Mn–BPY mixed characters, the 31a′ LUMO being localized more on the BPY ligand (68%) than the 30a′ HOMO (57%). Table 12 and Fig. 9 document that the 32a′ LUMO + 1 is largely composed by another, higher-lying π*(BPY) orbital. The three lower-lying occupied orbitals, 22a″ HOMO − 1, 29a′ HOMO − 2 and 28a′ HOMO − 3, are delocalized over the $\{Mn(CO)_3\}$ moiety.

The experimental UV–vis spectrum of $[Mn(CO)_3(BPY)]^-$ (Fig. 10, inset) shows in the visible area an intense absorption band at 547 nm, with several much less intense shoulders on both the higher and lower-energy sides. A medium-intensity absorption band appears at 352 nm. This spectroscopic pattern is reproduced appreciably well by the TD-DFT calculations (Fig. 10 and Table 14). Based on the computed results, the prominent visible absorption band originates from an electronic transition with a substantial 30a′ HOMO → 32a′ LUMO + 1 character and a small contribution from the 30a′ HOMO → 31a′ LUMO excitation. This largely MLCT/LLCT (Mn(CO) → BPY) transition is complementary to the lowest-energy one; however, the dominant 30a′ HOMO → 31a′ LUMO component gives the lowest-lying excited state only a limited charge transfer character. The higher-lying transition (better reproduced by ADF/BP) is nearly exclusively 30a′ HOMO → 23a″ LUMO + 2, again with a considerable MLCT/LLCT character. Our calculated spectrum reproduces also the small shoulder at 465 nm that is related to three separate MLCT/LLCT electronic excitations originating mainly from the 22a″ HOMO − 1, which is a largely d(Mn) orbital. We can conclude that despite the similar strongly delocalized nature of the π-bonding in the Mn(α-diimine) chelate ring of $[Mn(CO)_3(\alpha\text{-diimine})]^-$, reflected in their frontier orbitals, the electronic absorption spectra in the visible absorption region may strongly differ. The HOMO to HOMO − 4 char-

Table 13
One-electron energies and percentage composition of selected highest occupied and low-lying unoccupied molecular orbitals of $[Mn(CO)_3(BPY)]^-$ expressed in terms of composing fragments

MO	*E* (eV)	Mn	BPY	CO$_{ap}$	CO$_{bas}$
Empty					
24a″	2.28	7(p_z); 29(d_{xz})	19	13	31
23a″	1.56	1(d_{yz})	96	1	2
32a′	1.53	3(p_x); 1(d_{z^2}); 6($d_{x^2-y^2}$); 5(d_{xy})	74 (π*)	4	5
31a′	1.06	5(p_x); 2(d_{z^2}); 10($d_{x^2-y^2}$); 4(d_{xy})	68 (π*)	4	7
Occupied					
30a′	−0.14	9(p_x); 4(d_{z^2}); 14($d_{x^2-y^2}$); 2(d_{xy})	57 (π*)	2	12
22a″	−1.27	2(p_z); 60(d_z)	8	17	12
29a′	−1.52	2(p_x); 24(d_{z^2}); 1($d_{x^2-y^2}$); 37(d_{xy})	4	9	21
28a′	−1.66	2(p_y); 31(d_{z^2}); 15($d_{x^2-y^2}$); 18(d_{xy})	1	6	25
21a″	−2.71	1(d_{xz})	98 (π)		

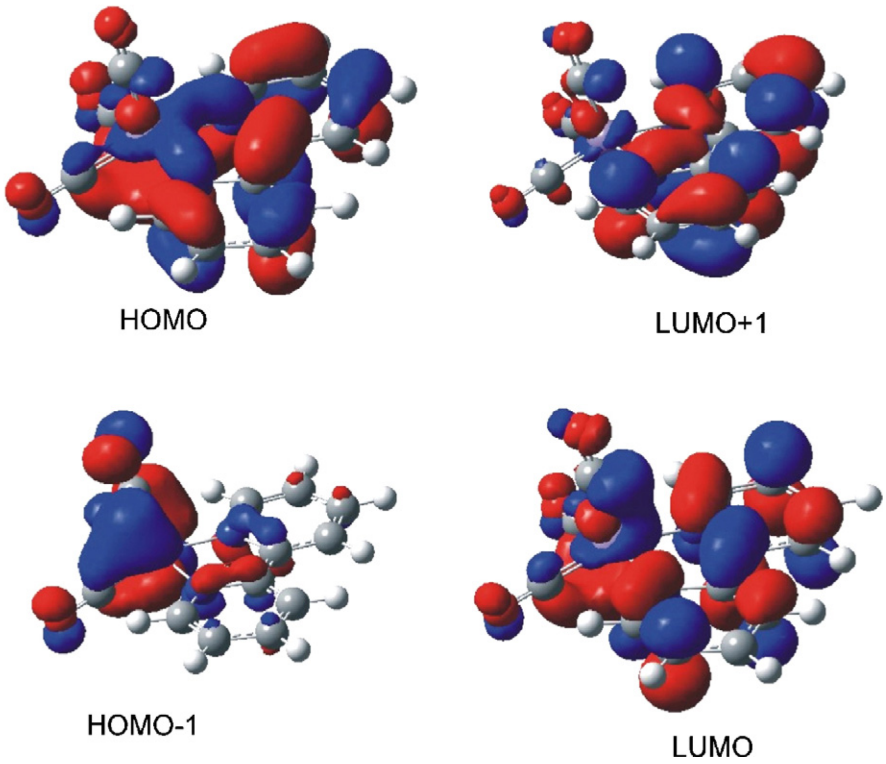

Fig. 9. The representation of the HOMO − 1 to LUMO + 1 of $[Mn(CO)_3(BPY)]^-$.

acters of $[Mn(CO)_3(\alpha\text{-diimine})]^-$ (α-diimine = R-DAB, BPY) are very close (Tables 6 and 13). The determining factor is then the difference in the number, symmetry and energy between the low-lying empty π^*(α-diimine) orbitals. The major influence of the α-diimine ligand on the spectroscopic pattern is apparent from the close correspondence between the UV–vis spectra of the five-coordinate complexes $[Mn(CO)_3(BPY)]^-$, $[Re(CO)_3(BPY)]^-$ (Refs. [30,31]) (also computed by TD-DFT [34]) and $[Ru(Me)(CO)_2(BPY)]^-$ (ref. [39]).

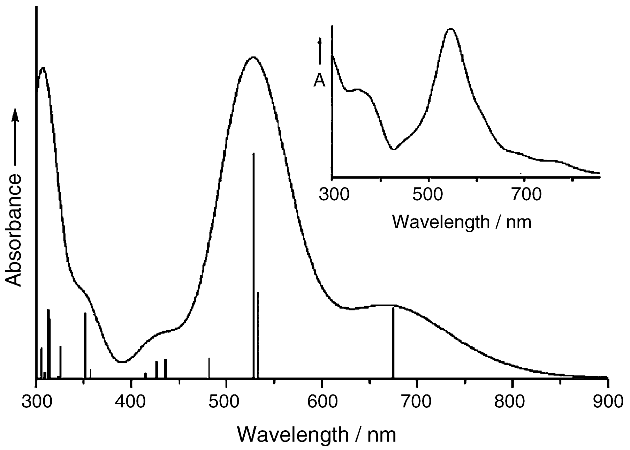

Fig. 10. The simulated electronic absorption spectrum of $[Mn(CO)_3(BPY)]^-$ based on G03/B3LYP calculated excitation energies and oscillator strengths (represented by vertical lines). Inset: the experimental electronic absorption spectrum of $[Mn(CO)_3(BPY)]^-$ in THF/10^{-1} M Bu_4NPF_6 at 293 K.

2.4. $[Mn(CO)_3(TMBP)]^-$ (TMBP = 4,4′,5,5′-tetramethyl-2,2′-biphosphinine)

The ground-state bonding properties and Kohn-Sham molecular orbitals, excited states and electronic absorptions spectra of the five-coordinate complex $[Mn(CO)_3(TMBP)]^-$ have been analyzed in detail in our previous report [29]. The frontier orbitals are depicted in Fig. 11. The molecular orbital diagrams of $[Mn(CO)_3(L_2)]^-$ (L_2 = BPY, TMBP) are qualitatively very similar, only the LUMO + 1 and LUMO + 2 characters are interchanged [29]. Despite the HOMO of $[Mn(CO)_3(TMBP)]^-$ is stabilized by 0.8 eV compared to that of the BPY complex, it remains strongly π-delocalized (Table 15). The calculated π HOMO character is in agreement with the stable five-coordinate geometry of $[Mn(CO)_3(TMBP)]^-$ in the presence of Lewis bases as well as with a large delocalization of π-bonding within the Mn–TMBP metallacycle revealed by crystallographic data. The different HOMO energies are reflected in the oxidation potentials of $[Mn(CO)_3(L_2)]^-$: −1.53 V for L_2 = BPY [27] but only −0.97 V for L_2 = TMBP [29] (THF, 293 K). The LUMO of $[Mn(CO)_3(TMBP)]^-$ lies only ca. 0.3 eV lower in energy than that of the BPY complex, having a nearly exclusive π^*(TMBP) character (Table 15). Differently from $[Mn(CO)_3(BPY)]^-$, the lowest-energy electronic transition of $[Mn(CO)_3(TMBP)]^-$ consists almost exclusively from a single excitation, viz. 36a′ HOMO → 37a′ LUMO, manifesting itself as a medium-intensity broad absorption band at 540 nm (Table 16). It has therefore a considerable MLCT/LLCT (i.e., (CO)Mn → TMBP) character, which also applies for other

Table 14
Selected TD-DFT calculated lowest-lying singlet excitation energies for $[Mn(CO)_3(BPY)]^-$ with oscillator strength (O.S.) larger than 0.005

State	Composition (ADF/BP)	ADF/BP		G03/B3LYP		Exp.	
		Transition energy (eV)	O.S.	Transition energy (eV)	O.S.	Transition energy (eV)	ε_{max} ($M^{-1}\,cm^{-1}$)
$^1A'$	67% $(30a' \rightarrow 31a')$	1.54	0.010	1.84	0.043	1.69	1700
	32% $(30a' \rightarrow 32a')$					1.83	sh
$^1A''$	92% $(30a' \rightarrow 23a'')$	2.05	0.039	2.33	0.053	2.04	sh
$^1A'$	60% $(30a' \rightarrow 32a')$	2.27	0.117	2.35	0.137	2.26	11300
	26% $(30a' \rightarrow 31a')$						
$^1A'$	84% $(22a'' \rightarrow 31a')$	2.43	0.013	2.58	0.012	2.66	sh
$^1A'$	54% $(30a' \rightarrow 33a')$	2.92	0.015	2.85	0.012		
	36% $(22a'' \rightarrow 23a'')$						
$^1A'$	46% $(22a'' \rightarrow 23a'')$	3.00	0.058	2.90	0.010		
	38% $(30a' \rightarrow 33a')$					3.51	7000
$^1A'$	50% $(28a' \rightarrow 32a')$	3.31	0.050	3.55	0.040		
	31% $(29a' \rightarrow 32a')$						
$^1A''$	66% $(30a' \rightarrow 25a'')$	3.37	0.091	3.82	0.020		
	13% $(21a'' \rightarrow 31a')$						

significant electronic transitions in $[Mn(CO)_3(TMBP)]^-$ in the visible and near-UV spectroscopic region (Table 15). The higher-lying, predominantly $28a''$ HOMO − 1 → $37a'$ LUMO transition probably also contributes to this absorption band. The prominent asymmetric absorption band at 411 nm arises due to two close-lying electronic transitions of similar intensities, viz. $36a'$ HOMO → $29a''$ LUMO + 1 and $36a'$ HOMO → $38a'$ LUMO + 2, both with ca 20% contributions from other excitations originating in the $28a''$ HOMO − 1. Finally, a group of similar, strongly mixed MLCT/LLCT electronic transitions is responsible for the intense absorption below 400 nm, with the maximum absorbance at 320 nm.

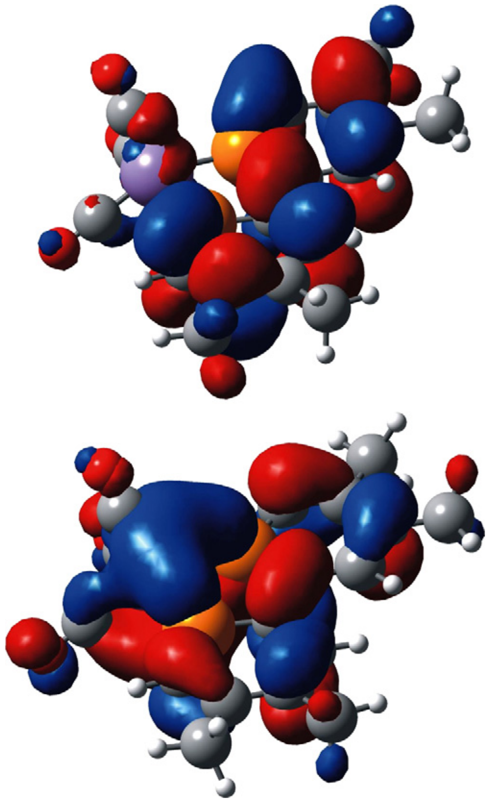

Fig. 11. The representation of the HOMO (bottom) and LUMO (top) of $[Mn(CO)_3(TMBP)]^-$.

Comparison of the electronic absorption spectrum of $[Mn(CO)_3(BPY)]^-$ in the preceding section with that of $[Mn(CO)_3(TMBP)]^-$ (ref. [29]) reveals similar spectroscopic patterns in the visible region, in agreement with the similar nature of molecular orbitals and electronic transitions involved. The corresponding absorption bands of $[Mn(CO)_3(TMBP)]^-$ are shifted to shorter wavelengths. The origin of this shift mainly lies in the large relative stabilization of the HOMO of the latter complex compared to that of $[Mn(CO)_3(BPY)]^-$, both orbitals being heavily involved in all electronic transitions in the visible spectroscopic region. The $\pi^*(L_2)$ contribution to the HOMO is around 50% in both complexes. This behavior agrees with the stronger electron-withdrawing nature of the neutral TMBP ligand compared to that of BPY [29].

2.5. $[Mn(CO)_3(1,2\text{-}S,S\text{-}C_6H_4)]^-$ (1,2-S,S-C_6H_4 = benzene-1,2-dithiolate)

The first attempt to compute the anion $[Mn(CO)_3(1,2\text{-}S,S\text{-}C_6H_4)]^-$ using ab initio and DFT methods dates back to 1999 (ref. [18]). The geometry of the anion was optimized on the Hartree-Fock and MP2 levels of theory. The coordination sphere of Mn is again a transition between square pyramid and trigonal bipyramid. The calculated Mulliken charge distribution has been in favor of the Mn(I) oxidation state of the metal center, similar to $[Mn(CO)_3(tBu\text{-}CAT)]^-$ (Section 2.1). The slightly lower CO stretching frequencies of $[Mn(CO)_3(1,2\text{-}S,S\text{-}C_6H_4)]^-$(1986(vs) and 1887(s,br) cm^{-1} in THF, 293 K) [18] compared to $[Mn(CO)_3(tBu\text{-}CAT)]^-$ (1994 and 1891 cm^{-1})

Table 15
ADF/BP calculated one-electron energies and percentage composition of selected occupied and unoccupied frontier molecular orbitals of $[Mn(CO)_3(TMBP)]^-$, expressed in terms of the constituent fragments (%) [29]

MO	*E* (eV)	Mn	TMBP	CO_{ap}	CO_{bas}
Empty					
30a″	2.18	2(p_z); 24(p_{xz})	35	6	27
38a′	1.37	3(p_y); 2(d_{z^2}); 4($d_{x^2-y^2}$); 15(d_{xy})	60	4	10
29a″	1.33	3(d_{xz}); 2(d_{yz})	93		2
37a′	0.79	1($d_{x^2-y^2}$); 1(d_{xy})	96 (π^*)		1
Occupied					
36a′	−0.94	9(p_y); 7(d_{z^2}); 13($d_{x^2-y^2}$); 3(d_{xy})	49 (π^*)	2	16
28a″	−1.50	2(p_z); 2(d_{xz}); 40(d_{yz})	36 (π)	11	8
35a′	−1.78	4(p_x); 15(d_{z^2}); 40(d_{xy})	12	15	14
34a′	−2.29	1(p_x); 46(d_{z^2}); 13($d_{x^2-y^2}$); 2(d_{xy})	11	0	25
27a″	−2.37	2(p_z); 16(d_{yz})	71 (π)	6	5

Table 16
Calculated lowest-lying TD DFT singlet excitation energies (eV) for $[Mn(CO)_3(TMPB)]^-$ with oscillator strength (O.S.) larger than 0.002 (ref. [29])

State	Composition (ADF/BP)	ADF/BP		G03/B3LYP		Exp.	
		Transition energy (eV)	O.S.	Transition energy (eV)	O.S.	Transition energy (eV)	ε_{max} (M^{-1} cm^{-1})
$^1A'$	94% (36a′ → 37a′)	1.87	0.009	2.20	0.025	2.29	2400
$^1A''$	71% (28a″ → 37a′) 28% (36a′ → 29a″)	2.43	0.003	2.68	0.011		
$^1A''$	61% (36a′ → 29a″) 21% (28a″ → 37a′)	2.72	0.084	2.87	0.094	3.02	15000
$^1A'$	71% (36a′ → 38a′) 22% (28a″ → 29a″)	2.78	0.064	2.93	0.088		
$^1A'$	51% (28a″ → 29a″) 32% (35a′ → 38a′)	3.29	0.091	3.45	0.117		
$^1A'$	55% (35a′ → 38a′) 15% (28a″ → 29a″)	3.60	0.113	3.73	0.117	3.86	
$^1A''$	34% (34a′ → 29a″) 24% (27a″ → 38a′)	3.74	0.199	3.92	0.094		

[21,24] point to a stronger π-donation from the dithiolate ligand and higher electron density at the Mn-carbonyl moiety than in the catecholate complex. The geometry of $[Mn(CO)_3(1,2\text{-S,S-}C_6H_4)]^-$ is qualitatively well described by our DFT calculations (Table 17), both methods slightly overestimating the Mn–S bond lengths.

Table 17
The comparison of experimental and DFT calculated selected bond lengths (Å) and angles of $[Mn(CO)_3(1,2\text{-S,S-}C_6H_4)]^-$

Bond	ADF/BP	G03/B3LYP	Exp.[a]
Mn–S	2.262	2.267	2.230
Mn–C(CO)$_{ap}$	1.757	1.785	1.750
Mn–C(CO)$_{bas}$	1.791	1.791	1.775
S1–C4	1.754	1.748	1.732
C4–C9	1.416	1.414	1.392
C–C(Ph)$_{av}$	1.403	1.400	1.382
C–O(CO)$_{av}$	1.174	1.165	1.164
S1–Mn–S2	87.7	87.9	87.8
Mn–S1–C4	107.7	106.3	107.0

[a] Experimental structure averaged in C_s symmetry [18].

The composition and energies of the Kohn-Sham molecular orbitals of $[Mn(CO)_3(1,2\text{-S,S-}C_6H_4)]^-$ are presented in Table 18. The 17a″ HOMO (π) of the complex (Fig. 12) indeed resides less on the bidentate ligand than that of $[Mn(CO)_3(t\text{Bu-CAT})]^-$ (Table 2 and Fig. 3), in agreement with the higher IR CO-stretching frequencies of the latter complex (see above). The LUMO (π^*) characters in these two five-coordinate complexes are very similar. Contrary to this, the 26a′ HOMO − 1 is localized more on the dithiolate ligand, which is compensated by the smaller dithiolate contribution to the 24a′ HOMO − 3. The 18a″ LUMO + 1 and 29a′ LUMO + 3 are largely localized on the {Mn(CO)$_3$} moiety. In general, the highest occupied and low-lying empty molecular orbital sets of $[Mn(CO)_3(1,2\text{-S,S-}C_6H_4)]^-$ and $[Mn(CO)_3(t\text{Bu-CAT})]^-$ are comparable. The only exception is the low-lying 28a′ LUMO + 2 of the former complex, which fully resides on the dithiolate ligand. The bonding in the Mn(dithiolate) chelate ring can be classified as more delocalized than in Mn(catecholate), in agreement with the trends presented in Introduction for the other complex series.

The electronic absorption spectrum of $[Mn(CO)_3(1,2\text{-S,S-}C_6H_4)]^-$ shows in the visible part three absorption bands of

Table 18
One-electron energies and percentage composition of selected highest occupied and lowest unoccupied molecular orbitals of $[Mn(CO)_3(1,2\text{-}S,S\text{-}C_6H_4)]^-$ expressed in terms of composing fragments

MO	E (eV)	Mn	S,S-C_6H_4	CO_{ap}	CO_{bas}
Empty					
29a′	2.33	2(p_y); 14(d_{z^2}); 11($d_{x^2-y^2}$)	5	11	56
28a′	1.86	1(d_{yz})	97	1	1
18a″	1.85	6(p_z); 30(d_{yz})	26	8	28
27a′	0.48	12(p_x); 3(d_{z^2}); 5($d_{x^2-y^2}$); 30(d_{xy})	27 (π^*)	10	13
Occupied					
17a″	−1.56	1(p_z); 30(d_{xz}); 1(d_{yz})	52 (π^*)	9	6
26a′	−1.77	8(p_x); 12(d_{z^2}); 10($d_{x^2-y^2}$)	53 (π)	1	15
25a′	−2.28	1(p_y); 42(d_{z^2}); 9($d_{x^2-y^2}$); 8(d_{xy})	15	0	23
24a′	−2.37	3(p_y); 21($d_{x^2-y^2}$); 26(d_{xy})	26	15	8
16a″	−2.59	3(p_z); 6(d_{xz})	68 (π)	7	5

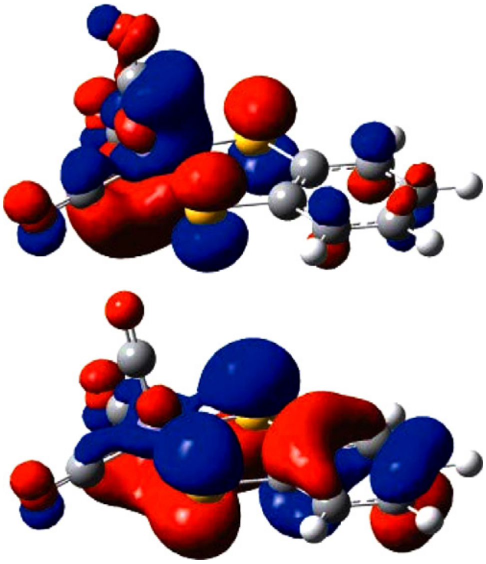

Fig. 12. The representation of the HOMO (bottom) and LUMO (top) of $[Mn(CO)_3(1,2\text{-}S,S\text{-}C_6H_4)]^-$.

medium to low intensities (Table 19) [18]. The most intense band at 400 nm belongs to an electronic transition with a dominant contribution from the 24a′ HOMO − 3 → 27a′ LUMO excitation and a minor 25a′ HOMO − 2 → 27a′ LUMO contribution. This transition has a negligible charge-transfer character, corresponding mainly to redistribution of the electron density within the $\{Mn(CO)_3\}$ moiety. The two lower-lying electronic transitions are also directed to the 27a′ LUMO (Fig. 12). The lowest-energy one, originating in the 17a″ HOMO, can be attributed a partial LMCT (dithiolate → Mn(CO)) character. This HOMO → LUMO transition is symmetry-forbidden, which explains its small oscillator strength and the low molar absorption coefficient of the corresponding absorption band at 552 nm (Table 19). The higher-lying 26a′ HOMO − 1 → 27a′ LUMO transition also corresponds a to partial dithiolate → Mn(CO) charge transfer (LMCT), giving rise to the absorption band at 502 nm. Apparently, the low-lying electron transitions computed for $[Mn(CO)_3(1,2\text{-}S,S\text{-}C_6H_4)]^-$ are dominated by a single one-electron excitation, in contrast to those of more strongly absorbing $[Mn(CO)_3(Me\text{-}CAT)]^-$ (Table 3). Their common feature is the partial LMCT nature of the lowest-energy excited states.

2.6. *$[Mn(CO)_3(1,2\text{-}S,NH\text{-}C_6H_4)]^-$ (1,2-S,NH-C_6H_4 = 2-thiolatophenylamido)*

The optimized structure of the last electronically unsaturated complex in the studied series, $[Mn(CO)_3(1,2\text{-}S,NH\text{-}C_6H_4)]^-$ (Table 20) agrees again very well with the experimental one [17], reproducing the distorted tetragonal pyramidal coordination environment of the Mn center. Protonation of the amide site is known to labilize the $[S\text{-}C_6H_4\text{-}NH]^-$ ligand and promote coordination of the fourth CO ligand. This reactivity demonstrates the strong π-donor ability of the chelating ligand stabilizing the five-coordinate geometry, which is also reflected in the short Mn–S and Mn–N bonds [17].

Table 19
Calculated lowest-lying TD DFT excitation energies (eV) for $[Mn(CO)_3(1,2\text{-}S,S\text{-}C_6H_4)]^-$ with oscillator strength (O.S.) larger than 0.005

State	Composition (ADF/BP)	ADF/BP		G03/B3LYP		Experiment[a]	
		Transition energy (eV)	O.S.	Transition energy (eV)	O.S.	Transition energy (eV)	ε_{max} (M^{-1} cm^{-1})
$^1A''$	97% (17a″ → 27a′)	2.33	0.012	2.30	0.008	2.24	1556
$^1A'$	97% (26a′ → 27a′)	2.72	0.077	2.67	0.032	2.47	2109
$^1A'$	68% (24a′ → 27a′) 10% (25a′ → 27a′)	3.25	0.053	2.76	0.020	3.10	4569
$^1A'$	61% (17a″ → 19a″) 13% (26a′ → 28a′)	3.97	0.139	3.43	0.138	3.55	2079

[a] In THF at 293 K [18].

Table 20
Comparison of experimental and DFT calculated selected bond lengths (Å) and angles of $[Mn(CO)_3(1,2\text{-}S,NH\text{-}C_6H_4)]^-$

Bond	ADF/BP	G03/B3LYP	Exp.[a]
Mn–S	2.286	2.328	2.268
Mn–N	1.937	1.910	1.889
$Mn–C(CO)_{ap}$	1.757	1.780	1.753
$Mn–C(CO)_{bas}$	1.786	1.791	1.761/1.776
S–C4	1.748	1.740	1.714
N–C9	1.363	1.371	1.375
C4–C9	1.424	1.420	
$C–C(Ph)_{av}$	1.402	1.400	
$C–O(CO)_{av}$	1.175	1.160	1.159
S–Mn–N	82.8	82.8	83.4
Mn–S–C4	100.5	98.7	100.2
Mn–N–C9	124.8	125.6	124.2

[a] Experimental structure averaged in C_s symmetry [17].

Table 21
One-electron energies and percentage composition of selected highest occupied and lowest unoccupied molecular orbitals of $[Mn(CO)_3(1,2\text{-}S,NH\text{-}C_6H_4)]^-$ expressed in terms of composing fragments

MO	*E* (eV)	Mn	$S,NH–C_6H_4$	CO_{ap}	CO_{bas}
Empty					
47a	2.56	2(p); 27(d)	12	10	49
46a	2.44	3(p); 21(d)	15	15	46
45a	2.32	1(d)	94	1	3
44a	0.92	9(p); 40(d)	31 (π^*)	8	11
Occupied					
43a	−0.98	3(p); 39(d)	41 (π^*)	8	9
42a	−1.32	5(p); 33(d)	40 (π)	5	16
41a	−1.72	60(d)	8	0	30
40a	−1.88	2(p); 47(d)	25	13	11
39a	−2.33	1(p); 17(d)	70(π)	5	6

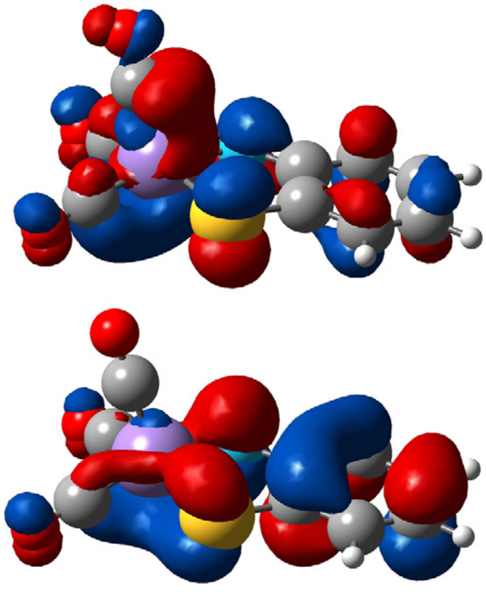
Fig. 13. The representation of the HOMO (bottom) and LUMO (top) of $[Mn(CO)_3(1,2\text{-}S,NH\text{-}C_6H_4)]^-$.

Inspection of Table 21 reveals completely delocalized nature of the frontier orbitals, the 43a HOMO and 44a LUMO (Fig. 13). The increased electron density on the Mn center in comparison with $[Mn(CO)_3(1,2\text{-}S,S\text{-}C_6H_4)]^-$ (Table 18), as judged on grounds of the HOMO characters, is also reflected in the stronger Mn → CO π-back-donation. This trend agrees with the lower IR CO-stretching frequencies of $[Mn(CO)_3(1,2\text{-}S,NH\text{-}C_6H_4)]^-$ (1973(vs) and 1870(s,br) cm^{-1} in THF, 293 K) [17] compared to $[Mn(CO)_3(1,2\text{-}S,S\text{-}C_6H_4)]^-$ (see above). The purely ligand-based 28a′ LUMO + 2 of $[Mn(CO)_3(1,2\text{-}S,S\text{-}C_6H_4)]^-$ has its equivalent in the 45a LUMO + 1 of $[Mn(CO)_3(1,2\text{-}S,NH\text{-}C_6H_4)]^-$. The 46a LUMO + 2 and 47a LUMO + 3 are largely localized on the carbonyl ligands.

According to our TD-DFT calculations, the lowest-energy absorption band of $[Mn(CO)_3(1,2\text{-}S,NH\text{-}C_6H_4)]^-$ at 500 nm originates almost exclusively in the 43a HOMO → 44a LUMO transition (Table 22). The HOMO-LUMO gap in this case (1.90 eV) is smaller than that for $[Mn(CO)_3(1,2\text{-}S,S\text{-}C_6H_4)]^-$ (2.04 eV). However, the latter complex shows the band due to the HOMO → LUMO transition red-shifted to 552 nm. This discrepancy may reflect the stronger π-delocalization within the $Mn(1,2\text{-}S,NH\text{-}C_6H_4)$ metallacycle. The lowest-energy absorption band of the asymmetric complex $[Mn(CO)_3(1,2\text{-}S,NH\text{-}C_6H_4)]^-$ is considerably more intense compared to that of $[Mn(CO)_3(1,2\text{-}S,S\text{-}C_6H_4)]^-$, where the corresponding electronic transition is symmetry-forbidden (see above).

The more intense visible absorption band of $[Mn(CO)_3(1,2\text{-}S,NH\text{-}C_6H_4)]^-$ at 402 nm is attributed to two electronic transitions (Table 22). The dominant one calculated at 3.32 eV (ADF)-3.37 eV (G03) involves the couple 41a HOMO − 2/40a

Table 22
Calculated lowest-lying TD DFT singlet excitation energies (eV) for $[Mn(CO)_3(1,2\text{-}S,NH\text{-}C_6H_4)]^-$ with oscillator strength (O.S.) larger than 0.005

State	Composition (ADF/BP)	ADF/BP		G03/B3LYP		Experiment[a]	
		Transition energy (eV)	O.S.	Transition energy (eV)	O.S.	Transition energy (eV)	ε_{max} (M^{-1} cm^{-1})
^1A	92% (43a → 44a)	2.27	0.022	2.55	0.034	2.48	6639
^1A	81% (42a → 44a) 9% (40a → 44a)	2.68	0.057	2.64	0.005		
^1A	57% (40a → 44a) 16% (41a → 44a)	3.32	0.088	3.37	0.179	3.08	9745
^1A	74% (43a → 46a) 8% (43a → 47a)	3.56	0.027	3.89	0.010		

[a] In THF at 293 K [17].

HOMO − 3 as starting states and the 44a LUMO as the arriving state. The major contribution from the 40a → 44a excitation gives this electronic transition only a limited MLCT/LLCT ((CO)Mn → 1,2-S,NH-C_6H_4) character, similar to the description of the intense 400-nm absorption band of the dithiolate complex (see above).

3. Concluding remarks

The noteworthy feature of this work is the detailed insight from the DFT calculations into the intriguing electronic structure of this series of five-coordinate, electron-deficient complexes $[Mn(CO)_3(L_2)]^-$ containing a variety of non-innocent chelating ligands L_2. All electronic transitions in the visible spectroscopic region have been thoroughly analyzed with TD-DFT and assigned successfully in terms of one-electron excitations. As predicted from experimental (spectroscopic, crystallographic, electrochemical) data and reactivity, the complexes exhibit a different degree of π-delocalization the MnL_2 metallacycle stabilizing the five-coordinate geometry, which is particularly well reflected in the DFT-computed characters of the highest occupied molecular orbital (π HOMO). The three lower-lying occupied orbitals, HOMO − 1 to HOMO − 3, were attributed in the literature [18,24,42] predominant d(Mn) characters (see Fig. 1). The computed data presented in this review clearly document that the former description of these orbitals has been oversimplified, neglecting the substantial contributions of carbonyl or L_2 (π^* and π) orbitals. The characters of the low-lying unoccupied molecular orbitals also vary significantly along the series studied. The π^* LUMO is often complementary to the π HOMO, ranging from largely carbonyl-Mn localized (L_2 = R-CAT) to strongly delocalized (L_2 = R-DAB), depending on the relative energies of the $\{Mn(CO)_3\}$ and L_2 based orbitals involved in the π-bonding delocalized over the $Mn(L_2)$ metallacycle. A different situation is encountered, however, for aromatic ligands like TMBP or BPY featuring a set of closely spaced low-lying π^* orbitals.

Comparison of the complexes $[Mn(CO)_3(R\text{-}DAB)]^-$ and $[Fe(CO)_3(R\text{-}DAB)]$ reveals that they can be treated as isoelectronic, strongly π-delocalized compounds. Stabilization of the iron valence orbitals causes less delocalized π-bonding in the chelate ring compared to the manganese center, the HOMO having a stronger carbonyl-Fe character and the LUMO being more localized on the R-DAB ligand.

The peculiar mixing of the metal, carbonyl and chelating-ligand contributions in the high-lying occupied and low-lying empty molecular orbitals of $[Mn(CO)_3(L_2)]^-$ and $[Fe(CO)_3(R\text{-}DAB)]$ together with the distorted geometry of the complexes makes the general discussion and comparison of their electronic absorption spectra an uneasy task. Each compound in the series in fact demands separate treatment and description. The common feature of the electronic transitions in the visible spectroscopic region is their limited or completely absent charge transfer character, in line with the lack of solvatochromism. This property is probably responsible for the excellent agreement between their computed and experimental energies obtained without the need to include the solvent environment in the TD-DFT calculations, which is important for charge-transfer electronic transitions [50].

4. Experimental

Diethyl ether (Et_2O) and dimethoxyethane (DME) of analytical grade (both Acros Chimica) were distilled freshly from sodium benzophenone. The precursor complex $[MnBr(CO)_3(BPY)]$ was prepared according to a published procedure [51].

4.1. Synthesis of $[Mn(CO)_3(BPY)]^-$ as a sodium salt

In a glove-box, a freshly prepared solution of sodium naphthalenide (10 mL, 0.6 mmol) in DME was added at room temperature to a solution of $[MnBr(CO)_3(BPY)]$ (113 mg, 0.3 mmol). The resulting violet solution was stirred for 5 min and the solvent was evaporated. The black solid obtained was washed with dry Et_2O (5 mL) and then dried under vacuum for 12 h to remove traces of remaining naphthalene. Part of the solid (ca. 10 mg) and Et_2O (2 mL) were sealed in a tube that was then heated at 35 °C at a water bath and gradually cooled down to room temperature (12 h). During this time, dark red plate crystals grew up inside the tube. ^1H and ^{13}C NMR measurements revealed that one molecule of free 2,2′-bipyridine was produced upon the reduction at room temperature. According to the NMR data, the solution contains a mixture of 2,2′-bipyridine and the anionic monomer $Na[Mn(CO)_3(BPY)]$. The NMR signals of free 2,2′-bipyridine were assigned by comparison with literature data [52]. In the crystalline state, the free 2,2′-bipyridine molecule chelates the Na^+ counterion. $Na[Mn(CO)_3(BPY)]$ was found to be too oxygen and moisture-sensitive to give satisfactory elemental analysis data.

^1H NMR (THF-d_8, 25 °C): δ 5.87 (m, 2H, $H_{5,5'}$), 6.38 (m, 2H, $H_{4,4'}$), 7.49 (m, 2H, $H_{3,3'}$), 9.34 (m, 2H, $H_{6,6'}$). ^{13}C NMR (THF, 25 °C): δ 109.55 (s, $C_{5,5'}$), 118.40 (s, $C_{4,4'}$), 121.25 (s, $C_{3,3'}$), 139.40 (s, $C_{2,2'}$), 154.05 (s, $C_{6,6'}$), 237.50 (s, CO).

The NMR spectra were recorded on a Bruker AC-220 SY spectrometer operating at 200.12 MHz for ^1H and 50.32 MHz for ^{13}C nuclei. Solvents peaks served as internal references relative to Me_4Si at 0 ppm.

4.2. X-ray structural determination

Dark red plates of the extremely air-sensitive complex $Na[Mn(CO)_3(BPY)]$ were obtained by slow cooling of a solution in Et_2O from 35 °C to room temperature. The tube was broken in a gloevbox, and crystals were protected with Paratone oil for handling on a Nonius Kappa CCD diffractometer using a Mo Kα (λ = 0.71069 Å) X-ray source and a graphite monochromator at 150 K. The crystal structures were solved using SIR 97 (ref. [53]) and SHELXL-97 (ref. [54]). ORTEP drawings were made using ORTEP III for Windows [55]. CCDC-295444 contains the supplementary crystallographic data. These data can be obtained free of charge at www.ccdc.cam.ac.uk/conts/retrieving.html [or from the Cambridge Crystallographic Data Center, 12 Union Road, Cambridge CB2 1EZ, UK; Fax: (internet.) +44 1223/336 033; E-mail: deposit@ccdc.cam.ac.uk].

4.3. DFT and TD DFT calculations

The ground-state electronic structures of the studied complexes $[Mn(CO)_3(L_2)]^-$ and $[Fe(CO)_3(Me\text{-}DAB)]$ were calculated by DFT methods, using Amsterdam Density Functional [56,57] (ADF2005.01) and Gaussian 03 (ref. [58]) software packages, with the exception of $L_2 = TMBP$. The complex $[Mn(CO)_3(TMBP)]^-$ was calculated earlier with ADF2000.2 and Gaussian 98, as described elsewhere [29]. When possible, the calculations were done in constrained C_s symmetry, with the metal center and C_{ap} located in the plane of symmetry.

Within the ADF program Slater type orbital (STO) basis sets of triple-ζ quality with one polarization function for H, C, N and O atoms and triple-ζ quality with additional two polarization functions for S, Mn and Fe were employed. Inner shells were represented by the frozen core approximation (1s for C, N, O; 1s, 2s, 2p for S, Mn and Fe). Within the ADF program, the functional including Becke's gradient correction [59] to the local exchange expression in conjunction with Perdew's gradient correction [60] to local density approximation (LDA) with Vosko-Wilk-Nusair (VWN) parametrization [61] of electron-gas data (ADF/BP), was used. Within Gaussian03, B3LYP hybrid functional [62] were used together with $6\text{–}31G^*$ polarized double-ζ basis sets [63,64] for H, C, N, O, S, Fe and Mn atoms (G03/B3LYP). The vibrational analyses were done with the "pure" density functional BPW91 [59,65], using structures optimized with this functional.

The low-lying excited states of closed-shell complexes were calculated using the TD-DFT method (both ADF/BP and G03/B3LYP). The electronic absorption spectra were simulated using the GaussSum software [66].

The substituents on the *i*Pr-DAB and *t*Bu-CAT ligands were modelled by the methyl group (Me-DAB) and (Me-CAT). The vibrational analyses of $[Mn(CO)_3(i\text{Pr-DAB})]^-$ and $[Mn(CO)_3(t\text{Bu-CAT})]^-$ were done for the real complexes.

Acknowledgements

Dr. Brenda D. Rossenaar (University of Amsterdam and AKZO Nobel, Arnhem) recorded the resonance Raman spectrum of the complex $[Mn(CO)_3(i\text{Pr-DAB})]^-$. We thank Prof. Antonín Vlček (University of London) for stimulating discussions and continued interest in this work. Financial support was provided by the Council for Chemical Sciences of the Netherlands Organization for Scientific Research (CW-NWO, travel grant No. R 71-140), the CNRS and École Polytechnique, and the COST Actions D14 and D35 that were also supported by the Ministry of Education of the Czech Republic (grant No. 1P05OC68). The Grant Agency of the Academy of Sciences of the Czech Republic (S.Z., grant No. 1ET400400413) is also gratefully acknowledged.

References

[1] W. Ponikwar, P. Meyer, W. Beck, Eur. J. Inorg. Chem. (2002) 1932, and references therein.
[2] S. Greulich, W. Kaim, A.F. Stange, H. Stoll, J. Fiedler, S. Záliš, Inorg. Chem. 35 (1996) 3998.
[3] A.S. Goldman, J. Halpern, J. Organomet. Chem. 382 (1990) 237.
[4] D.A. Lunder, E.B. Lobkowsky, W.E. Streib, K.G. Caulton, J. Am. Chem. Soc. 113 (1991) 1837.
[5] S.A. Macgregor, D. MacQueen, Inorg. Chem. 38 (1999) 4868.
[6] A. Kovacs, G. Frenking, Organometallics 20 (2001) 2510.
[7] M.P. Wilms, E.J. Baerends, A. Rosa, D. Stufkens, J. Inorg. Chem. 36 (1997) 1541.
[8] S.A. Decker, M. Klobukowski, J. Am. Chem. Soc. 120 (1998) 9342.
[9] D. Sellmann, W. Ludwig, G. Huttner, L. Zsolnai, J. Organomet. Chem. 294 (1985) 199.
[10] D. Sellmann, M. Wille, F. Knoch, Inorg. Chem. 32 (1993) 2534.
[11] D.J. Darensbourg, K.K. Klausmeyer, B.L. Mueller, J.H. Reibenspies, Angew. Chem. Int. Ed. Engl. 31 (1992) 1503.
[12] D.J. Darensbourg, K.K. Klausmeyer, J.H. Reibenspies, Inorg. Chem. 34 (1995) 4676.
[13] D.J. Darensbourg, K.K. Klausmeyer, J.H. Reibenspies, Inorg. Chem. 35 (1996) 1529.
[14] D.J. Darensbourg, K.K. Klausmeyer, J.H. Reibenspies, Inorg. Chem. 35 (1996) 1535.
[15] D.J. Darensbourg, J.D. Draper, B.J. Frost, J.H. Reibenspies, Inorg. Chem. 38 (1999) 4705.
[16] F. Hartl, Unpublished results.
[17] W.-F. Liaw, C.-M. Lee, G.-H. Lee, S.-M. Peng, Inorg. Chem. 37 (1998) 6396.
[18] C.-M. Lee, G.-Y. Lin, C.-H. Hsieh, C.-H. Hu, G.-H. Lee, S.-M. Peng, W.-F. Liaw, J. Chem. Soc., Dalton Trans. (1999) 2393.
[19] W.-F. Liaw, C.-K. Hsieh, G.-Y. Lin, G.-H. Lee, Inorg. Chem. 40 (2001) 3468.
[20] M. Oh, G.B. Carpenter, D.A. Sweigart, Organometallics 21 (2002) 1290.
[21] F. Hartl, A. Vlček Jr., L.A. deLearie, C.G. Pierpont, Inorg. Chem. 29 (1990) 1073.
[22] F. Hartl, A. Vlček Jr., Inorg. Chem. 30 (1991) 3048.
[23] M. Krejčík, M. Daněk, F. Hartl, J. Electroanal. Chem. Interfacial Electrochem. 317 (1991) 179.
[24] F. Hartl, D.J. Stufkens, Vlček Jr., A Inorg. Chem. 31 (1992) 1687.
[25] F. Hartl, Inorg. Chim. Acta 268 (1998) 1.
[26] F. Hartl, A. Vlček Jr., Inorg. Chem. 31 (1992) 2869.
[27] F. Hartl, B.D. Rossenaar, G.J. Stor, D.J. Stufkens, Recl. Trav. Chim. Pays-Bas 114 (1995) 565.
[28] B.D. Rossenaar, F. Hartl, D.J. Stufkens, C. Amatore, E. Maisonhaute, J.-N. Verpeaux, Organometallics 16 (1997) 4675.
[29] F. Hartl, T. Mahabiersing, P. Le Floch, F. Mathey, L. Ricard, P. Rosa, S. Záliš, Inorg. Chem. 42 (2003) 4442.
[30] (a) G.J. Stor, F. Hartl, J.W.M. van Outersterp, D.J. Stufkens, Organometallics 14 (1995) 1115;
(b) B.D. Rossenaar, F. Hartl, D.J. Stufkens, Inorg. Chem. 35 (1996) 6194.
[31] Y.F. Lee, J.R. Kirchhoff, R.M. Berger, D. Gosztola, J. Chem. Soc., Dalton Trans. (1995) 3677.
[32] F.P.A. Johnson, M.W. George, F. Hartl, J.J. Turner, Organometallics 15 (1996) 3374, and references therein.
[33] J.W.M. van Outersterp, F. Hartl, D.J. Stufkens, Organometallics 14 (1995) 3303.
[34] E. Fujita, J.T. Muckerman, Inorg. Chem. 43 (2004) 7636.
[35] W.-F. Liaw, N.-H. Lee, C.-H. Chen, C.-M. Lee, G.-H. Lee, S.-M. Peng, J. Am. Chem. Soc. 122 (2000) 488.
[36] W.-F. Liaw, J.-H. Lee, H.-B. Gau, C.-H. Chen, S.-J. Jung, C.-H. Hung, W.-Y. Chen, C.-H. Hu, G.-H. Lee, J. Am. Chem. Soc. 124 (2002) 1680.
[37] M.P. Aarnts, F. Hartl, K. Peelen, D.J. Stufkens, C. Amatore, J.-N. Verpeaux, Organometallics 16 (1997) 4686.
[38] J. van Slageren, F. Hartl, D.J. Stufkens, Eur. J. Inorg. Chem. (2000) 847.
[39] F. Hartl, M.P. Aarnts, H.A. Nieuwenhuis, J. van Slageren, Coord. Chem. Rev. 230 (2002) 107.
[40] D.J. Stufkens, Coord. Chem. Rev. 104 (1990) 39, and references therein.
[41] P. Barbaro, C. Bianchini, K. Linn, C. Mealli, A. Meli, F. Vizza, F. Laschi, P. Zanello, Inorg. Chim. Acta 198–200 (1992) 31.

[42] F. Hartl, P. Barbaro, I.M. Bell, R.J.H. Clark, T.L. Snoeck, A. Vlček Jr., Inorg. Chim. Acta 252 (1996) 157, and references therein.

[43] M.W. Kokkes, D.J. Stufkens, A. Oskam, J. Chem. Soc., Dalton Trans. (1983) 439.

[44] T.A. Albright, J.K. Burdett, M.-H. Whangbo, Orbital Interactions in Chemistry, Wiley-Interscience, New York, 1985.

[45] B.D. Rossenaar, Ph.D. Thesis, University of Amsterdam, 1995.

[46] L. Luo, S.P. Nolan, Inorg. Chem. 32 (1993) 2410.

[47] R.K. Kochhar, R. Pettit, J. Organomet. Chem. 6 (1966) 272.

[48] R.W. Balk, D.J. Stufkens, A. Oskam, J. Chem. Soc., Dalton Trans. (1982) 275.

[49] G.J. Stor, D.J. Stufkens, P. Vernooijs, E.J. Baerends, J. Fraanje, K. Goubitz, Inorg. Chem. 34 (1995) 1588.

[50] A. Vlček Jr., S. Záliš, J. Phys. Chem. A 109 (2005) 2091.

[51] L.H. Staal, A. Oskam, K. Vrieze, J. Organomet. Chem. 170 (1979) 235.

[52] M.J. Cook, A.P. Lewis, G.S.G. McAuliffe, Org. Magn. Reson. 22 (1984) 388.

[53] A. Altomare, M.C. Burla, M. Camalli, G. Cascarano, C. Giacovazzo, A. Guagliardi, A.G.G. Moliterni, G. Polidori, R. Spagna, SIR97, an integrated package of computer programs for the solution and refinement of crystal structures using single-crystal data, 1999.

[54] G.M. Sheldrick, SHELXL-97, Universität Göttingen, Göttingen, 1997.

[55] L.J. Farrugia, J. Appl. Crystallogr. 30 (1997) 565.

[56] G. G te Velde, F.M. Bickelhaupt, S.J.A. van Gisbergen, C. Fonseca Guerra, E.J. Baerends, J.G. Snijders, T.J. Ziegler Comput. Chem. 2001 22, 931.

[57] ADF2005.01, SCM, Theoretical Chemistry, Vrije Universiteit, Amsterdam, http://www.scm.com.

[58] M.J. Frisch, G.W. Trucks, H.B. Schlegel, G.E. Scuseria, M.A. Robb, J.R. Cheeseman, J.A. Montgomery Jr., T. Vreven, K.N. Kudin, J.C. Burant, J.M. Millam, S.S. Iyengar, J. Tomasi, V. Barone, B. Mennucci, M. Cossi, G. Scalmani, N. Rega, G.A. Petersson, H. Nakatsuji, M. Hada, M. Ehara, K. Toyota, R. Fukuda, J. Hasegawa, M. Ishida, T. Nakajima, Y. Honda, O. Kitao, H. Nakai, M. Klene, X. Li, J.E. Knox, H.P. Hratchian, J.B. Cross, V. Bakken, C. Adamo, J. Jaramillo, R. Gomperts, R.E. Stratmann, O. Yazyev, A.J. Austin, R. Cammi, C. Pomelli, J.W. Ochterski, P.Y. Ayala, K. Morokuma, G.A. Voth, P. Salvador, J.J. Dannenberg, V.G. Zakrzewski, S. Dapprich, A.D. Daniels, M.C. Strain, O. Farkas, D.K. Malick, A.D. Rabuck, K. Raghavachari, J.B. Foresman, J.V. Ortiz, Q. Cui, A.G. Baboul, S. Clifford, J. Cioslowski, B.B. Stefanov, G. Liu, A. Liashenko, P. Piskorz, I. Komaromi, R.L. Martin, D.J. Fox, T. Keith, M.A. Al-Laham, C.Y. Peng, A. Nanayakkara, M. Challacombe, P.M.W. Gill, B. Johnson, W. Chen, M.W. Wong, C. Gonzalez, J.A. Pople, Gaussian 03, revision C.02, Gaussian Inc., Wallingford, CT, 2004.

[59] A.D. Becke, Phys. Rev. A 38 (1988) 3098.

[60] (a) J.P. Perdew, Phys. Rev. B 33 (1986) 8822;
(b) J.P. Perdew, Phys. Rev. B 34 (1986) 7406 (erratum).

[61] S.H. Vosko, L. Wilk, M. Nusair, Can. J. Phys. 58 (1980) 1200.

[62] P.J. Stephens, F.J. Devlin, C.F. Cabalowski, M.J. Frisch, J. Phys. Chem. 98 (1994) 11623.

[63] P.C. Hariharan, J.A. Pople, Theo. Chim. Acta 28 (1973) 213.

[64] V.A. Rassolov, J.A. Pople, M.A. Ratner, T.L. Windus, J. Chem. Phys. 109 (1998) 1223.

[65] J.P. Perdew, Y. Wang, Phys. Rev. B 45 (1992) 13244.

[66] N.M. O'Boyle, J.G. Vos, GaussSum 1.0, Dublin City University, 2005.